CALIBRATION OF AND ATTITUDE ERROR ESTIMATION FOR A SPACEBORNE SCATTEROMETER USING MEASUREMENTS OVER LAND

Clarence J. Wilson III

Department of Electrical and Computer Engineering

M.S. Degree, March 30, 1998

ABSTRACT

The NASA Scatterometer (NSCAT) was launched August 20, 1996 aboard the National Space Development Agency of Japan's Advanced Earth Observing Spacecraft (ADEOS). NSCAT's primary mission was to measure radar backscatter over the world's oceans. These measurements are used to generate estimates of ocean wind speed and direction. Scatterometers must be calibrated before their measurements are scientifically useful. However, the calibration of NSCAT must be done in orbit. A new methodology for selecting land regions for use in extended target spaceborne scatterometer calibration is first developed. Next, a summary of the calibration technique used in this thesis is presented. While the foundation of this technique was previously developed theoretically, the work in this thesis is its first application for calibration/validation of an on-line spaceborne radar system. The technique is extended to estimate simultaneously NSCAT's calibration and the host spacecraft's attitude error. The attitude references reported by the attitude control system on-board ADEOS are deemed erroneous. Results of this expanded technique, applied under varying assumptions, are presented for consideration. A summary and suggestions for future research conclude this work.

COMMITTEE APPROVAL:

David G. Long, Committee Chairman

David V. Arnold, Committee Member

Wynn C. Stirling, Committee Member

Michael D. Rice , Graduate Coordinator

CALIBRATION OF AND ATTITUDE ERROR ESTIMATION FOR A SPACEBORNE SCATTEROMETER USING MEASUREMENTS OVER LAND

A Thesis
Submitted to the
Department of Electrical and Computer Engineering
Brigham Young University

In Partial Fulfillment
of the Requirements for the Degree
Master of Science

by
Clarence J. Wilson III
March 30, 1998

This thesis by Clarence J. Wilson III is accepted in its present form by the Department of Electrical and Computer Engineering of Brigham Young University as satisfying the thesis requirement for the degree of Master of Science.

David G. Long, Committee Chairman

David V. Arnold, Committee Member

Wynn C. Stirling, Committee Member

Date

Michael D. Rice , Graduate Coordinator

DEDICATION

The technical value of the contents are of little use to you, Kathy; nonetheless, I dedicate them with all my Love to you. Also, with love to our beloved children, Cal, Maddie, and whoever is coming next.

ACKNOWLEDGMENTS

I wish to acknowledge Dr. David Long's patience and dedication to helping me complete the thesis herein contained. I wish to thank him for his guidance and support. From before I began my graduate studies though the final weeks of writing, he has consistently urged me toward higher ground. His confidence in the ability of inexperienced undergraduate students to do necessary work in the near-term and meaningful work in the long-term, thus propelling them out of the crowded valley of the common and up the inclines of intellectual mountains, whose challenges are not little but whose views are not unremarkable; perhaps this is to what I am most indebted.

The association of one's peers and colleagues cannot be mentioned with emphasis sufficient for the treasure of discoveries, enlightenment, inspiration, and simple fun that are enjoyed among fellow travelers/adventurers. Thank you Travis Oliphant, Paul Johnson, Ryan Reed, and Quinn Remund.

I thank Rocky Mountain Space Grant Consortium for their financial support from September, 1995 through February, 1997.

I thank my supervisors at my current employer, Dynetics, Inc., of Huntsville, Alabama, for their support during the preparation of this manuscript. Finally, I thank the University of Alabama in Huntsville for use of computer facilities to aid in its completion.

Contents

List of Tables

List of Figures

Chapter 1

INTRODUCTION

The precise calibration of a spaceborne scatterometer radar directly impacts the scientific usefulness of the instrument's measurements. In order to successfully fulfill its mission, the measurement error due to system biases must be minimized. Due to the difficulty of end-to-end calibration of spaceborne scatterometers before launch, thorough post-launch data calibration analyses are employed. Traditionally, these calibration analyses attempt to identify the relative biases among the multiple measurement subsystems associated with each of the instrument's beams. In past calibration efforts other system biases, such as those resulting from erroneous spacecraft attitude information, have not been thoroughly considered. In this thesis, a new method is presented for simultaneous calibration and estimation of spacecraft attitude errors for a spaceborne scatterometer radar.

1.1 A Brief Description of the Problem

The primary use of spaceborne scatterometers is to produce measurements that may be used to estimate the wind speed and direction over the oceans. For this purpose, the NASA scatterometer (NSCAT) was launched August 16, 1996 aboard the Japanese spacecraft known as the Advanced Earth Observing Satellite (ADEOS). In order to estimate wind speed and direction to within the accuracies required for NSCAT's mission, errors in measurement data due to instrumentation errors need to be reduced to only a few tenths of a decibel [1].

The bias due to instrumentation errors in uncalibrated measurement data falls into two categories: absolute and relative. The magnitude of absolute bias is impossible to determine during post-launch calibration efforts because no calibrated targets are available. Relative bias, also known as "interbeam" bias, results from differences among the several "beams" used to collect measurements. NSCAT has six different antenna which form eight beams (six vertical and two horizontal polarization). Each of the eight beams has a gain pattern which is different from the others, leading to different relative biases for each beam. An ideally calibrated scatterometer

accounts for these relative biases such that under equivalent measurement conditions each beam measures the same backscattered power from a given ground location.

In the midst of the ongoing post-launch calibration, it was discovered that the attitude information reported by the host spacecraft ADEOS was inaccurate. Due to this erroneous attitude information, the orientation of each NSCAT antenna differs from that used to calculate the normalized backscatter response. In effect, this induces a new bias in the measurement data which we refer to as "attitude bias". This attitude bias differs for each beam (due to their different deployment angles) and may vary throughout the spacecraft's orbit. Calibration of NSCAT thus requires not only the traditional relative bias corrections, but also corrections to account for biases associated with these attitude errors.

1.2 Basic Approach

The approach to the relative, or interbeam, calibration problem in this thesis is adapted from the work of Skouson and Long [2,3]. To attempt the attitude error estimation/correction problem, the theory is extended to include bias due to attitude error. Briefly, this approach equates the measured backscatter, σ°_{meas}, with the sum of the true backscatter, σ°_{tr}, the absolute bias, σ°_{abs}, the interbeam bias, σ°_{ibb}, and the attitude bias, σ°_{att}:

$$\sigma^\circ_{meas} = \sigma^\circ_{tr} + \sigma^\circ_{abs} + \sigma^\circ_{ibb} + \sigma^\circ_{att}. \tag{1.1}$$

This is complicated by several factors. Each of these quantities can be a non-linear function of incidence and azimuth angle. Also, they may be temporal functions of time of day (diurnal variations) and time of year (seasonal variations). Attitude bias, as mentioned before, can be a function of orbit latitude. To reduce the complexity of the problem, surface regions are selected which do not display variation with these parameters. Only measurement data from so-called "calibration regions" is then used to form the calibration estimates σ°_{ibb} and σ°_{att}.

1.3 Outline of Thesis

In this thesis, an approach to the calibration of and attitude estimation for a spaceborne scatterometer is presented. The contents both develop the theoretical foundation of this approach and present its results when applied in the NSCAT calibration campaign.

Chapter 2 presents background information on spaceborne scatterometers and their role in monitoring the ocean's surface winds. NSCAT's design is also discussed, especially as it impacts measurement calibration.

In Chapter 3, the methodology for the selection of the extended area calibration regions is discussed. Criteria for selecting such regions and our method of doing so are presented. As an example, the selection process is stepped through in detail for the Amazon rainforest region.

In Chapter 4, the technique for using measurement data from calibration regions to calibrate a spaceborne scatterometer is presented. This technique is a variation of that presented by Skouson and Long [2, 3].

In Chapter 5, the problem of attitude errors is discussed. An extension to the calibration technique is developed which simultaneously estimates attitude errors and interbeam biases.

In Chapter 6, the results of applying the technique are discussed. Trends are identified which appear in the estimates. Results are also presented of the same technique applied with slightly different assumptions.

Finally, Chapter 7 summarizes the conclusions of this work. A list of contributions made follows. Recommendations to future calibration efforts which must also estimate attitude errors is also included.

Chapter 2

BACKGROUND

In this chapter, background information is presented to aid in understanding the primary focus of this thesis. First, the theory of scatterometers, their role in ocean wind estimation, and the impact calibration has on the quality of such wind estimates are discussed. Next, the design of the instrument NSCAT is summarized. Finally, a summary is presented of what is meant by "calibration" in this thesis given the context of a spaceborne scatterometer.

The material in this section is intended only as a summary of the pertinent issues. For a more in-depth discussion, the following references are recommended. The standard reference on scatterometry and the field of remote sensing in general is Ulaby, Moore, and Fung [4]. Two important papers discussing the design of NSCAT are Naderi, Freilich, and Long [1] and Long, Chi, and Li [5]. Discussion on the calibration of previous scatterometers may be found in Bracalente *et. al.* [6], Long and Skouson [3], and Lecomte and Attema [7]. Less formal, but readily available, information on wind scatterometry and NASA's past, present, and planned spaceborne scatterometer projects may (currently) be found on the world wide web at URL `http://winds.jpl.nasa.gov` .

2.1 Scatterometers

A scatterometer is a radar designed to measure the backscattered power from relatively large surface areas. Like all radars, its power measurement is described by the radar equation:

$$P_S = \frac{G^2 \lambda^2 L_s A}{(4\pi)^3 R^4 G_p} \sigma^\circ P_T \tag{2.1}$$

where P_S is the backscattered signal power, G is the antenna gain (both transmit and receive), λ is the wavelength of the electromagnetic energy transmitted, A is the surface area of the observed location, L_s is the system loss, R is the range from the radar to the observed location, G_p is the processor gain, σ° is the normalized radar backscatter coefficient (or normalized radar cross section), and P_T is the transmit power. Note that the radar actually measures a returned power, P_R, which is the sum of the returned signal power and the noise power. Thus, P_S is given by $P_R - P_N$.

2.1.1 σ° and the X-Factor

The normalized radar backscatter coefficient, σ°, is often refered to simply as the "backscatter". σ° has been normalized by A, the area of the observed location. The product $A\sigma^\circ$ gives σ, the radar cross section (RCS) which is the terminology used in many other radar applications. σ is the area of an *isotropic* target that would reflect, or backscatter, the same return power, P_S, as the observed location does. Not surprisingly, σ, and thus σ°, are strong functions of the incidence angle of the radar beam with the observed location. They are also typically functions of azimuth angle, surface roughness, and the surface's electrical properties.

In scatterometry, the parameters of the radar equation are often collected under one term, called the "X-factor":

$$\sigma^\circ = XP_S \tag{2.2}$$

where

$$X = \frac{(4\pi)^3 R^4 G_p}{G^2 \lambda^2 A L_s P_T}. \tag{2.3}$$

The desired estimate, σ°, is directly related to the instrument's measurement, P_S. In theory, all of the parameters composing X may be calculated or otherwise obtained in a deterministic manner. However, in reality, they are subject to change and are only known with limited precision. Errors in the values of the parameters composing X thus lead to erroneous values of σ° [3].

2.1.2 Wind Retrieval

Scatterometer measurements over ocean surfaces may be used to form estimates of the near-surface wind speed and direction. Scatterometers primarily designed for this purpose (such as NSCAT) are called "wind scatterometers" and the process of estimating wind vectors is called "wind retrieval". The ability to retrieve wind vectors over the ocean's surface is of tremendous value to scientists developing and applying global numerical weather models to better understand and monitor the global climate and to predict future weather patterns accurately. Spaceborne wind scatterometers are uniquely capable of providing σ° measurements to retrieve wind vectors around the globe under all weather and cloud conditions. Further, they provide data with relatively high spatial resolution and frequent re-sampling [1].

The correlation between wind speed and direction with backscatter over the ocean's surface is not difficult to understand conceptually. Wind blowing over

the surface of the ocean forms waves, "roughening" the surface. The wind speed determines the extent to which the surface is roughened. Further, strong correlation exists between the direction of the waves and the direction of the wind. The amount of energy backscattered and observed by the radar is directly influenced by the roughness of the ocean surface and the direction of the waves. In general, at incidence angles away from normal, smooth surfaces backscatter little energy while rough surfaces backscatter more. Thus the observed backscatter can be used to estimate the wind.

Because the actual physical processes which correlate wind speed and direction to σ° measurements are extremely complex, expressions accurately relating them are not available. To overcome this shortcoming, empirical models have been developed based on data collected during previous scatterometer missions. These geophysical model functions yield a σ° value given the wind's speed and direction, the radar's incidence angle, θ, and its relative azimuth angle to the surface, ϕ (as well as other parameters such as wavelength and polarization). However, the incidence and relative azimuth angles are known and scatterometers provide σ°, so the wind retrieval problem is to then estimate the wind speed and direction based on the geophysical model function.

For a single measurement (σ°, θ, ϕ) over a given surface location all wind directions are possible at varying wind speeds. However, when several (3 or 4) completely error-free measurements of the same surface location are obtained at *different* azimuth angles, the wind speed and direction may be reduced to a solution set of up to four possibilities, or "ambiguities". Algorithms have been developed to select which of the wind vector ambiguities is most probable. Real scatterometer measurements, of course, are subject to errors. As a result, selecting the correct ambiguity becomes even more difficult. As the error in σ° measurements becomes large, the quality of the wind vector estimates becomes poor [1, 5].

2.1.3 The Need for Good Calibration

Measurement errors fall into three categories: communication error, instrumentation error (also known as retrieval error), and geophysical modeling error. The normalized variability of the σ° measurement error, K_P^2, is given by the sum of the squares of the respective normalized component variances [2, 3]:

$$K_P^2 = K_{P_c}^2 + K_{P_r}^2 + K_{P_m}^2. \tag{2.4}$$

Geophysical modeling error is a property of the surface and is not effected by the instrument. Communication error is determined by the instrument design and cannot be reduced after the instrument is deployed. However, the variability due to instrumentation or retrieval error, K_{P_r}, results from erroneous values for the parameters which comprise the X-factor. As mentioned earlier, this leads to biased σ° values.

The goal of calibrating a spaceborne scatterometer is to minimize the uncertainty and remove the bias in the X-factor, thus minimizing K_{P_r} and reducing the overall K_P [2, 3]. A well-calibrated scatterometer, then, is able to produce consistent, temporally stable σ° measurements from which high-quality wind vector estimates may be produced. Calibration is essential to successfully fulfilling the mission of a wind scatterometer to provide useful data for monitoring global ocean winds and their impact on our global climate.

2.2 NSCAT - A General Description

NSCAT is a Ku-band scatterometer radar operating at 13.955 GHz (λ=2.15 cm). It consists of six identical, dual-pol fan beam antennas approximately 10 feet long (see Fig. 2.1). Only two of the six antennas actually use both horizontal and vertical polarizations, the other four only use vertical (resulting in a total of 8 "beams"; see Fig. 2.2). The antennas are pointed at the Earth creating two parallel, 600 km-wide tracks below the spacecraft (one on either side) as it orbits the earth (see Fig. 2.3) [1].

To satisfy the scientific requirements of the mission, NSCAT must provide σ° measurements at a spatial resolution of 25 km-by-25 km [1]. To meet this requirement in the cross-track direction, each beam's footprint on the Earth's surface is separated into 24 "cells" based on the Doppler shift imposed by the relative motion of the Earth and the satellite. These Doppler cells provide 25 km resolution across the subtrack. In the along-track direction, the desired 25 km resolution is achieved by using a very narrow beamwidth (0.4°, 7–15 km on the surface). NSCAT cycles through its 8 beams sequentially every 3.74 seconds as the spacecraft moves through its orbit. This results in each beam's footprint moving 25 km every cycle [1].

The timing employed by NSCAT is based on the 3.74 s measurement cycle of the 8 beams. This allocates 468 ms to each beam. A burst of 25 pulses followed by 4 noise-only measurement intervals, each of duration 16 ms, comprises each beam's measurement frame. The 120 W (peak) transmit pulses are each 5.0 ms long

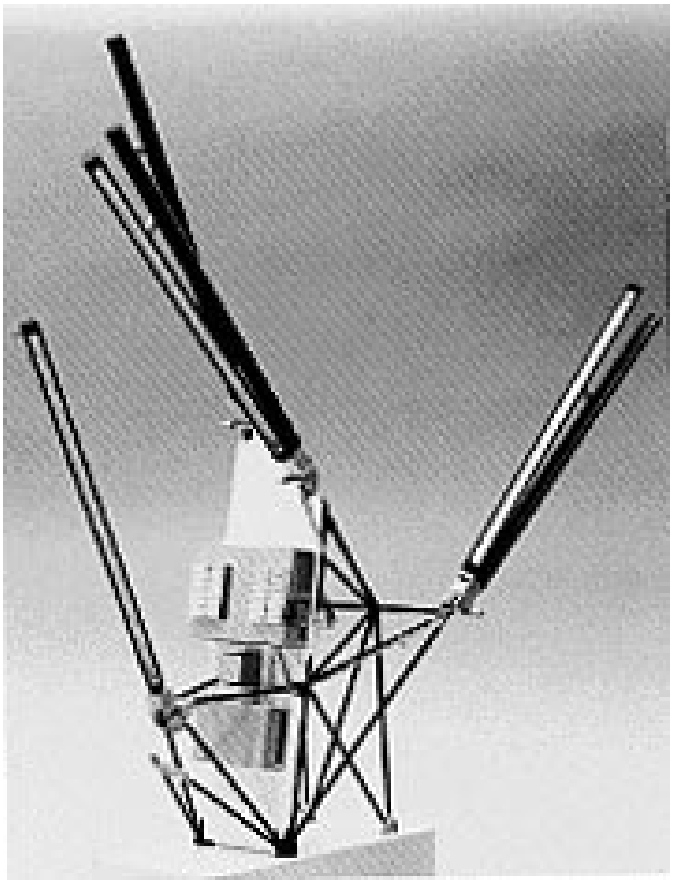

Figure 2.1: *A model of the NSCAT instrument before attachment to the ADEOS spacecraft.*

followed by an 11 ms receiving period (a 31% duty cycle at 62 Hz PRF). The noise-only measurements are subtracted from the signal+noise measurements to obtain the signal-only measurements required by the radar equation [1].

NSCAT's mission also requires it to cover 90% of the ice-free ocean every two days [1]. This is achieved by its 100.92 minute polar orbit (inclination 98.59°, altitude 796.75 km, ground speed 6.7 km/sec). This orbit yields 14.27 revolutions per day and repeats, or retraces itself, every 41 days. Generally, a given surface location is observed twice every day, once during an ascending pass and again approximately 11–13 hours later during a descending pass of the satellite (or vice versa).

2.2.1 NSCAT Backscatter Measurements

As mentioned above, NSCAT transmits 25 pulses during each beam's measurement frame. Each returned pulse is divided in the frequency domain to form 24

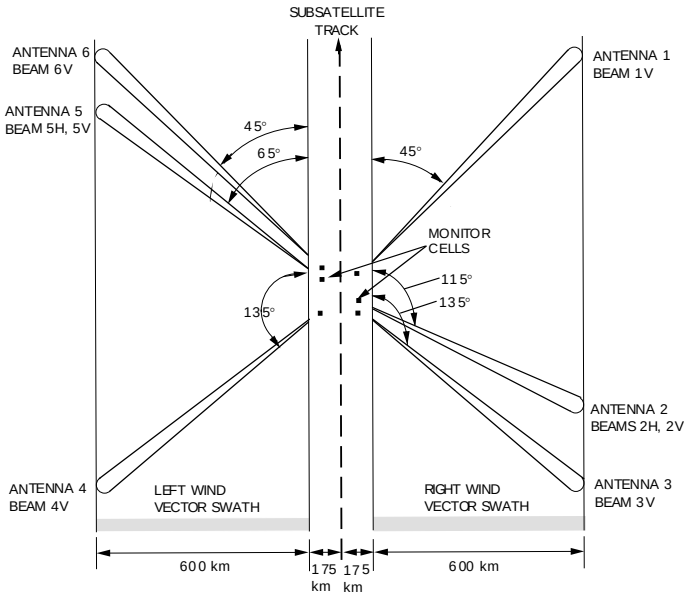

Figure 2.2: *A diagram showing NSCAT's 8 beams associated with its 6 antennas. The deployment angles of the antennas and the swaths that result are also displayed.*

Doppler cells. The frequency information corresponding to each Doppler cell is integrated from all 25 pulses to form the received signal+noise power (P_R) for each cell [1]. A detailed description of the digital signal processing techniques applied onboard NSCAT to form P_R may be found in [5]. After the noise-only power, P_N, is subtracted, the signal-only power, P_S, remains. Estimates of the parameters comprising the X-factor are then applied according to Equation 2.3 to obtain the backscatter, σ°, for each cell. Thus, during a single measurement frame for any given beam, 24 σ° values (one for each Doppler cell) are produced.

The scientific requirements of NSCAT's mission call for wind vector estimates whose accuracy is 2 m/s for speed and 20° for direction. To obtain these accuracies, NSCAT's σ° measurement error must be reduced to only a few tenths of a decibel [3]. These errors result from inaccuracies in the parameters forming the X-factor. Additionally, the process of forming the P_S values, as described above, contributes inaccuracy to the calculated σ° value.

2.3 Calibration of a Spaceborne Scatterometer

An ideally calibrated scatterometer accounts for all errors which add bias to its calculated σ° values. Two categories of such errors are defined: errors that affect all beams equally, and errors that affect beams differently. The resulting biases

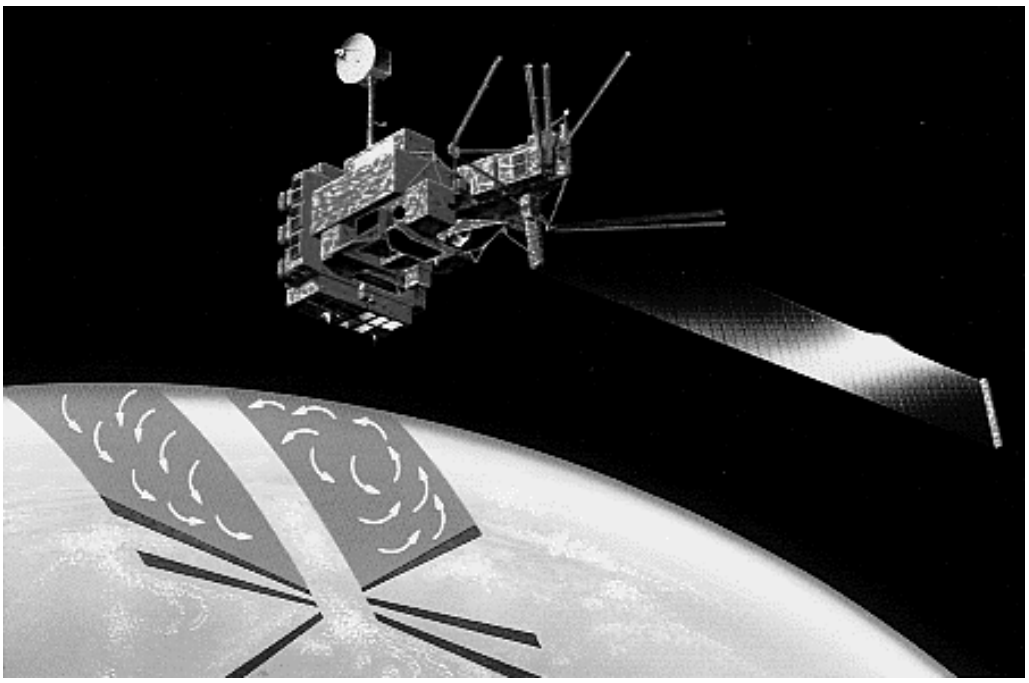

Figure 2.3: *The ADEOS spacecraft with NSCAT mounted aboard orbiting the Earth. The curly vectors on the Earth represent the wind vectors that are formed based on NSCAT data. The six antenna footprints are also apparent displaying the different azimuth angles from which each beam observes surface locations.*

of these two types of error sources are called, respectively, *absolute bias* and *relative bias*. Before the instrument is prepared for launch, a series of calibration experiments are conducted to remove as many biases as possible. However, these techniques are limited and cannot account for biases that may have changed when the instrument is placed in orbit and turned on. Thus, post-launch calibration is required [3].

During post-launch calibration, it is impossible to remove absolute bias because no calibrated targets are available. However, relative biases may still be identified and removed by carefully examining NSCAT's σ° measurement data. Relative biases may be due to differences among the antennas such as the antenna patterns, the RF path loss to each antenna, antenna pointing error, etc. Also, filters applied to each beam's measurements may differ slightly.

As will be discussed in Chapter 5, during the course of NSCAT's post-launch calibration, an additional source of relative bias was identified: spacecraft attitude error. Briefly, because the spacecraft's attitude determines how the antennas are pointed, parameters such as the range to the observed location, R, and the area of the observed location, A, are incorrect and contribute bias to each beam's σ°

value. Because the antennas are oriented differently, the parameters for each beam are affected differently leading to different biases imposed on each beam, that is, relative bias.

Because it is impossible to remove absolute bias after a spaceborne scatterometer is launched, the goal of post-launch calibration is to account for and minimize *relative* biases. Under equivalent measurement conditions, a scatterometer so calibrated will (ideally) measure the same normalized radar backscatter coefficient, σ°, from a given surface location with all of its beams.

Chapter 3

SELECTING CALIBRATION REGIONS

In this chapter, the process followed to find land regions suitable for use in the calibration process is presented. Criteria are listed which have been developed in previous calibration studies using land regions. Next, a description of the set of imagery used to identify and evaluate potential calibration regions is provided. The methodology employed to measure a candidate land regions' characteristics relative to the criteria follows. The process is demonstrated with the selection of a calibration region in the Amazon rainforest. Finally, a map of the world is presented and the calibration regions used in this thesis are identified along with an analysis of their validity from the viewpoint of scattering theory.

3.1 Criteria

Kennett and Li studied the use of land targets for scatterometer calibration. They developed several criteria for selecting land regions to be used in scatterometer calibration [8]. Their criteria suggested an ideal calibration region have:

- Mean σ° known at the frequencies, polarizations, and incidence angles of interest;
- Large spatial extent of the area to allow for a large number of measurements over a relatively short period of time;
- Spatial variations in σ° which are small and well understood;
- Interannual variations in σ° which are small and well understood;
- Diurnal variations in σ° which are small and well understood;
- Azimuth angle variations in σ° which are small and well understood; and,
- Target conditions which remain consistent over the extent of the calibration time period.

None of these ideal criteria may be completely satisfied because *a priori* knowledge of these properties does not exist for any region of the earth over any extended period of time. Indeed, research to collect and expand our understanding of the backscatter properties of the Earth's land regions at medium and low spatial resolutions is ongoing. Efforts by Kennett and Li [8, 9], Frison and Mougin [10], and Mougin et. al. [10] have begun this process. However, Kennett and Li's work was with SASS (a Ku-band scatterometer) which only collected data for about 3 months. Frison and Mougin's work was with ERS-1 scatterometer which operated at C-band, though it covers 3 years of data. As yet, there exists no catalog which defines regions acceptable for calibrating spaceborne Ku-band scatterometers based on the above criteria.

To overcome the lack of known calibration regions for Ku-band measurements, a simple bootstrap technique is employed to determine acceptable candidates. After a reasonable quantity of uncalibrated measurements is available, regions appearing to satisfy the above conditions are sought. Imagery produced using the SIRF algorithm (briefly described below) of all the land regions around the globe are created and studied to select candidates. Based on how well the above criteria are satisfied, such candidate study regions are then used in the calibration process.

3.2 SIRF Imagery

The Scatterometer Image Reconstruction with Filtering (SIRF) algorithm, developed by Long, Hardin, and Whiting [11], estimates two parameters of the backscatter response of an illuminated land region. These two parameters have been shown to well-describe and discriminate land regions with different types of vegetation [12, 13]. The SIRF algorithm models the land surface's backscatter response by

$$10\, log_{10}\sigma^{\circ} = \mathcal{A} + \mathcal{B}\,(\theta - 40^{\circ}). \tag{3.1}$$

SIRF uses σ° measurements of the same geographic location made at different incidence angles to form estimates of $\mathcal{A}$ and $\mathcal{B}$. SIRF is a nonlinear Multiplicative Algebraic Reconstruction Technique (MART). A detailed analysis of SIRF is found in [14].

Individual $\mathcal{A}$- and $\mathcal{B}$-values are estimated by SIRF for very small geographical areas ($\sim$ 20 km^2). The $\mathcal{A}$ and $\mathcal{B}$ estimates are used as pixel values to form greyscale images of large land regions. In this manner, so-called $\mathcal{A}$-images and $\mathcal{B}$-images of all the land regions throughout the world may be created.

3.3 Finding Land Calibration Targets

SIRF $\mathcal{A}$- and $\mathcal{B}$-images are used to locate extended spatial land targets whose temporal evolution is considered minimal. In order to evaluate the temporal evolution of such extended land targets, a time-series of SIRF imagery is created for the entire world. Each image in the time-series is formed from 10 days of NSCAT σ° measurement data. At the time of this work, data for seven such images was available. This data extends from September 15 through November 23, 1996 a period of significant seasonal change for much of the world. Assuming NSCAT's instrumentation is reasonably stable with respect to time, temporally stable calibration regions can be selected using this data.

3.3.1 Mean and Standard Deviation Images

For each land region around the world, a single (temporal) "mean image" is created from the seven time-series $\mathcal{A}$-images. The pixel values for this image are the averages of the corresponding pixel values of the time-series images. By visually analyzing such mean images, large spatially homogeneous areas with similar $\mathcal{A}$-values may be identified.

Similarly, a (temporal) standard deviation image is calculated for each land region around the world. Here, the pixels for this image represent the standard deviation of the corresponding pixels values of the time-series images. By looking at such standard deviation images, areas with little change over time may be identified.

Finally, calibration regions are chosen by identifying areas with both similar mean values and small standard deviations. These are found by first visually locating such areas and then using computer visualization tools to specifically identify the calibration region pixel by pixel.

Use of the first and second moments as a means of evaluating the properties of land regions' stability implies the assumption of a uni-modal distribution. Indeed, in this context, this assumption is made for every pixel location in the time-series of SIRF images. Though quite a broad assumption, it seems reasonable for land regions with stable responses. Unstable regions, on the other hand, may display multi-modal distributions with first and second moments outside the range of acceptable moments found in stable regions.

3.3.2 Searching for Calibration Regions in South America

To illustrate the process of selecting a calibration region, we examine the South American continent which contains the Amazon rainforest. The Amazon rainforest region has been suggested in all previous calibration efforts [3, 6, 8, 15] to be the most useful land calibration region in the world because of its extensive size, homogeneous backscatter characteristics (spatial and temporal), and apparent lack of azimuthal modulation.

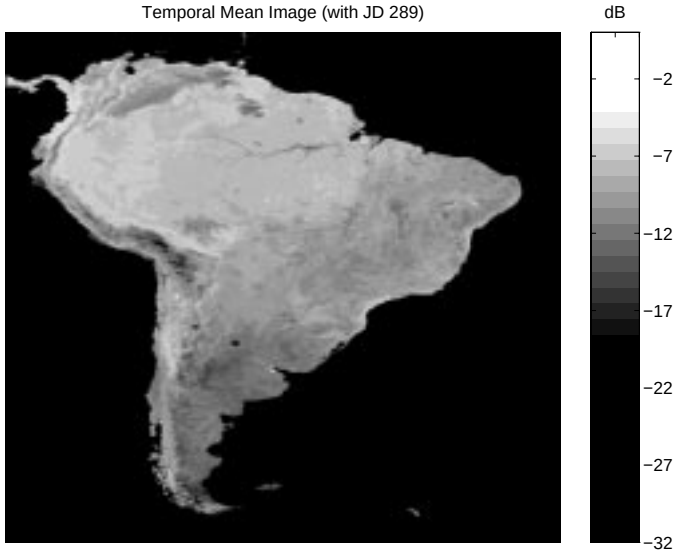

Figure 3.1: *Temporal mean A-image of South America using all available images.*

The first step is to create the time series of images covering South America. Next, the mean and standard deviation images are created (see Figures 3.1 and 3.2). Careful examination of the standard deviation image reveals a diagonal "spotting" pattern. Further investigation reveals that these "spots" occur as a result of missing data in the Julian Day (JD) 289-298 image (see Figure 3.3). NSCAT was turned off for a majority of this period of time (6 of 10 days) and so the σ° measurement coverage of the region was significantly reduced. The SIRF algorithm sets pixels with no measurements over them to a floor value (-32 dB), yielding corrupted pixels in the the time-series standard deviation image. To overcome this problem, new mean and standard deviation images are produced without the JD 289 image (see Figs. 3.4 and 3.5).

With the mean and standard deviation images available (Figs. 3.4 and 3.5), the search for calibration regions begins. Two likely areas are readily apparent to the

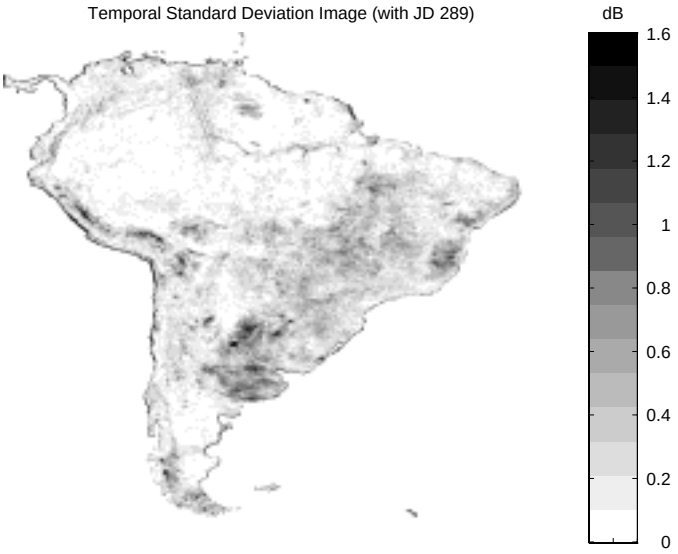

Figure 3.2: *Standard deviation $\mathcal{A}$-image of South America using all available images.*

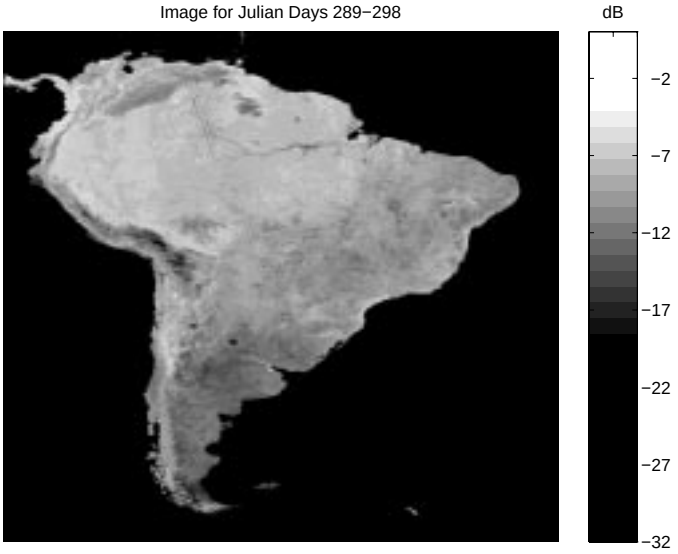

Figure 3.3: *SIRF $\mathcal{A}$-image of Julian Days 289-298. Note the "spotting" which passes diagonally through the continent.*

eye in the images. The Amazon rainforest, as previously suggested, appears to be an excellent calibration region. Its tremendous size, very low standard deviation over time, and small range of temporal mean values make it very appealing for calibration. The second area is found in the southern tip of the continent. This region, called

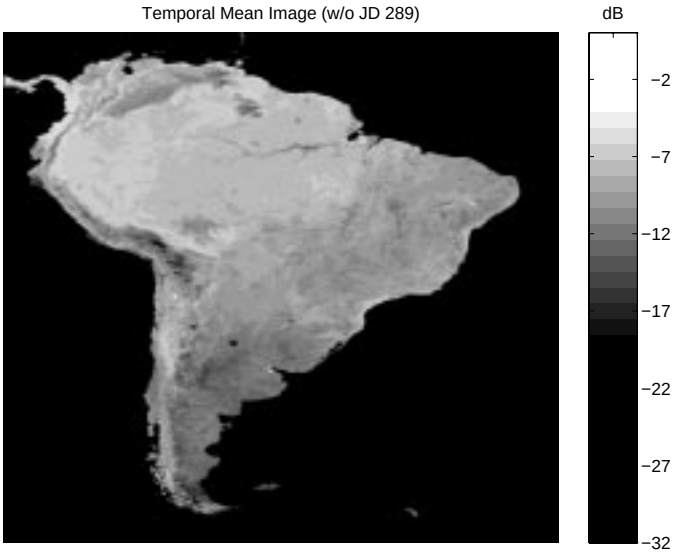

Figure 3.4: *Mean $\mathcal{A}$-image calculated without the JD 289 image.*

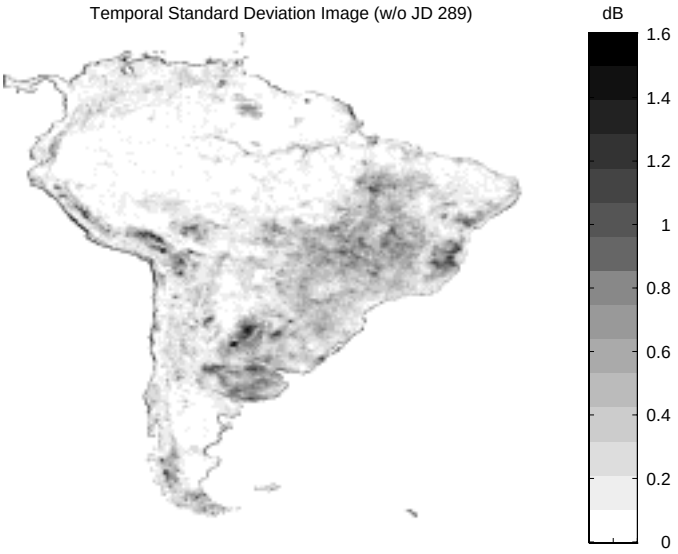

Figure 3.5: *Standard deviation $\mathcal{A}$-image calculated without the JD 289 image.*

Patagonia, also has a very low standard deviation and small range of mean values over a significant, though smaller, area.

The exact calibration regions are somewhat arbitrarily selected. They are defined by ranges of mean and standard deviation values. Locations whose mean and standard deviation images have values in both defined ranges are selected to be in the calibration region. The pixels corresponding to these locations form the so-called

"calibration mask". These ranges are parametrically varied until a mask deemed "best" is found. This decision is based primarily on visual inspection, though statistics of the mask's pixel values are used for comparison. Figure 3.6 shows the mask so selected for the Amazon rainforest. In this case, "best" is subjectively determined to be a temporal mean in the range -8 to -6 dB and a temporal standard deviation less than 0.3 dB.

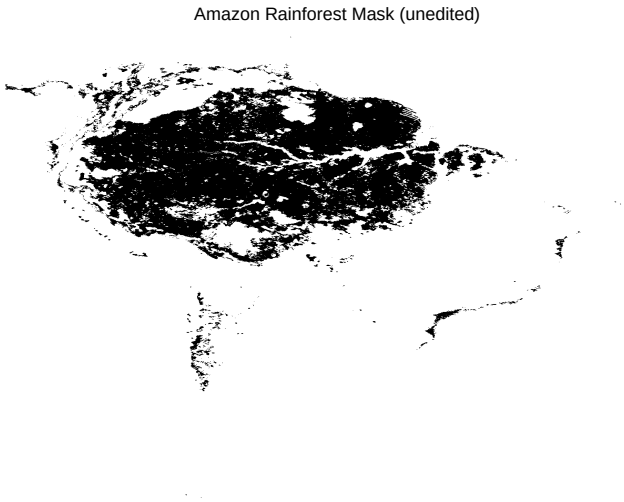

Figure 3.6: *Mask of Amazon rainforest produced by selecting pixels with (temporal) standard deviation < 0.3 dB and (temporal) mean between -8 and -6 dB.*

Two further editing operations are performed on the selected mask. First, areas determined not to be part of the vegetation region (the Amazon rainforest) are deleted from the mask. Thus, the mountainous and coastal regions which appear to have properties similar to the Amazon rainforest's are manually deleted. Second, because natural phenomena tend to display smooth spatial variations, small "holes" are filled and small "islands" deleted by applying a 3-by-3 median filter to the mask. Figure 3.7 is the final form of the Amazon mask after completing these "editing" operations enlarged to show detail.

The same procedure is repeated for the Patagonian region. Figure 3.8 is the mask created for this region. It is based on areas with a temporal mean between -13 and -11 dB and a temporal standard deviation less than 0.3 dB.

This process continues for all regions of the Earth's land surfaces. The mean and standard deviation $\mathcal{A}$-images of the entire world are presented in Figures 3.9 and 3.10. Each region of the Earth was carefully studied for suitability as a

calibration region. A total of seven calibration regions were initially formed, though two were later discarded when unsuitable properties were discovered. A collection of these calibration masks is found in Figure 3.11. The five calibration regions used in this thesis are refered to as follows: the Amazon rainforest, Patagonia, the Congo rainforest, the Indonesian rainforest, and Western Greenland.

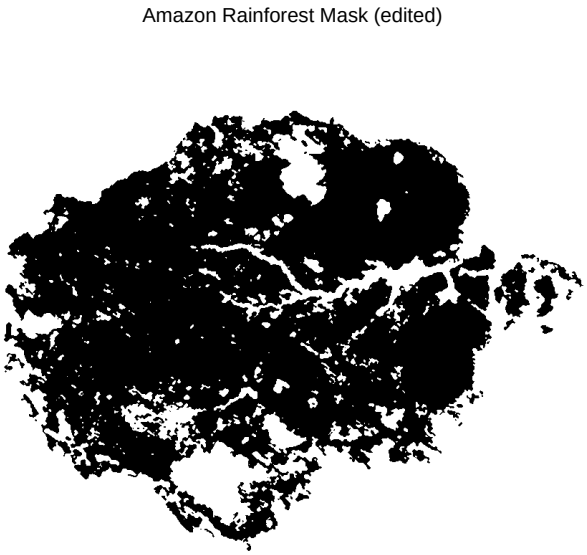

Figure 3.7: *Edited and final version of Amazon rainforest mask. Areas outside the Amazon rainforest have been removed and a 3-by-3 median filter applied.*

Figure 3.8: *Final version of Patagonia mask based on pixels with mean between -13 and -11 dB and standard deviation < .3 dB.*

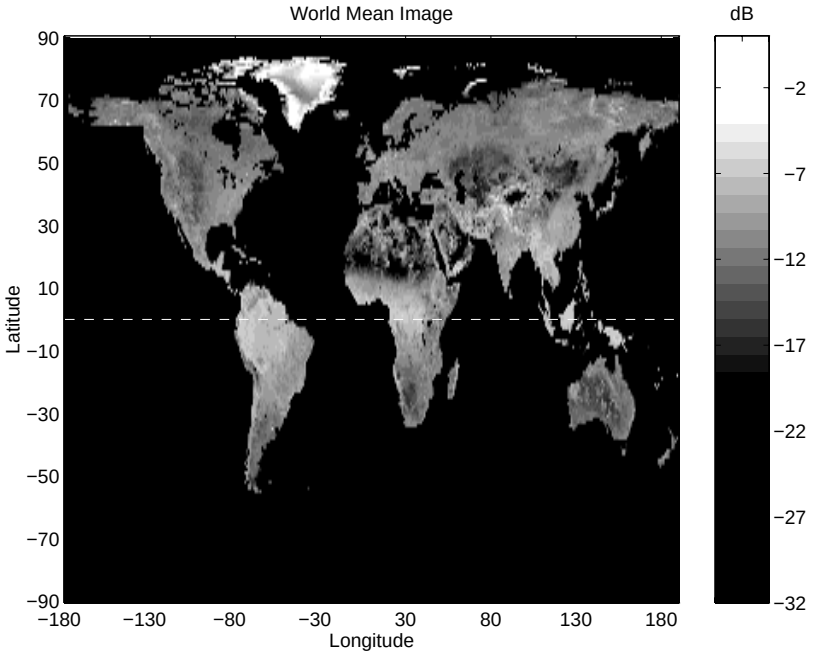

Figure 3.9: *Mean $\mathcal{A}$-image of the entire world.*

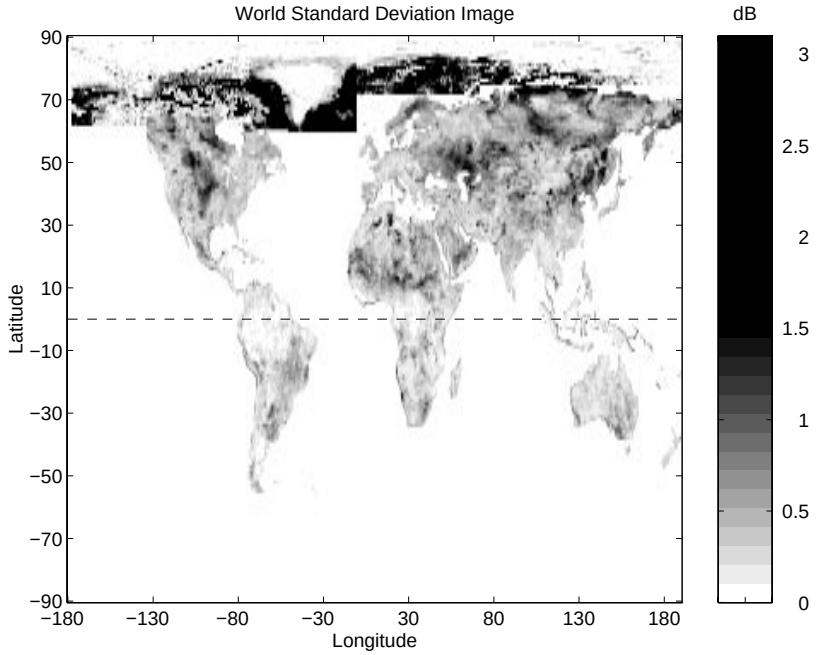

Figure 3.10: *Standard deviation $\mathcal{A}$-image of the entire world.*

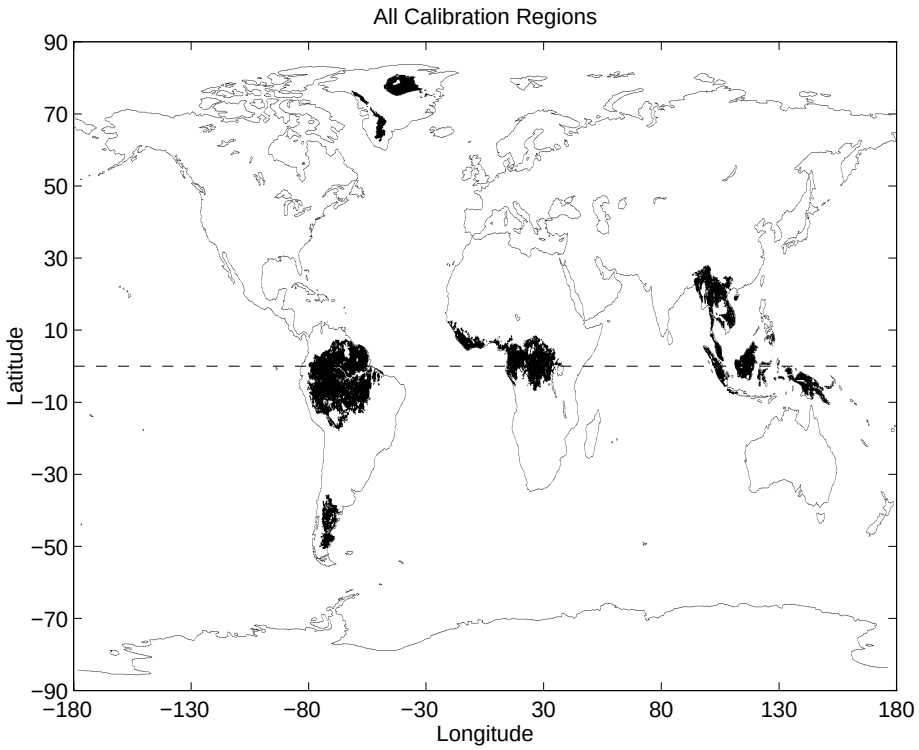

Figure 3.11: *Edited and final version of all the calibration region masks around the world. The regions are the Amazon rainforest, Patagonia, the Congo rainforest, the Indonesian rainforest, and Western Greenland. Also displayed are two masks which are not used: Northeast Greenland and Southeast Asia.*

3.4 Calibration Regions: Taking Another Look from the Point of View of Scattering Theory

Having selected calibration regions based solely on measurement data (in the form of $\mathcal{A}$- and $\mathcal{B}$- values), it is useful and prudent to review why these would be suitable before proceeding. Scattering theory describes the interaction of electromagnetic waves with many kinds of surfaces and materials. Scattering occurs when electromagnetic energy traveling in one medium encounters an interface with another medium. In scatterometry, this is typified by the electromagnetic wave traveling down through the air and encountering the Earth's surface, vegetation, a body of water, or man-made structures on the surface.

There are two types of scattering, "surface scattering" and "volume scattering". Surface scattering has a strong dependence on incidence angle at midrange values ($20^\circ - 60^\circ$). As the incidence angle increases, the backscattered energy decreases rapidly, depending on the surface roughness (rougher surfaces exhibit less incidence angle dependence). However, volume scattering occurs in the volume of the lower medium. Thus, it is not as strongly dependent upon incidence angle. In fact, it is nearly constant until the incidence angle reaches large values [4].

The calibration regions selected consist of three basic land forms. The Amazon, Congo, and Indonesia are all rainforests. Rainforests are characterized by a heavy vegetation canopy many meters thick. Greenland's surface consists of layers of snow and ice. Patagonia is a semi-arid desert with some shrubbery. All of these regions are relatively flat with spatially homogeneous features.

At Ku-band, scattering over the rainforests regions and Greenland is dominated by volume scattering. The rainforest's heavy canopy is also expected to show some *rough* surface scattering which is similar in nature to volume scattering. The canopy significantly attenuates the energy so surface scattering from the ground is minimized. Further, the random orientation of the scatterers in the canopy (leaves, branches, etc.) tends to minimize any azimuth angle dependence. Examination of the σ° properties of the Amazon rainforest and Greenland may be found in [12, 16]. Figures 3.12 thru 3.14 display typical σ°_{meas} for rainforests, snow and ice layers, and Patagonia desert.

The calibration regions selected are thus dominated by volume scattering and rough surface scattering. These classes of scattering tend to reduce the dependence of σ° on the local terrain. The effect is a relatively uniform σ° response over

the entire geographical region. Volume scattering also lends to temporal stability compared to surface scattering as its scattering region (the subsurface) is less prone to short-term changes compared to the "exposed" interface of surface scattering. Further, little seasonal change occurs to the calibration regions during the time of the data being used. These factors combine to form spatially and temporally homogeneous regions suitable for calibration analysis.

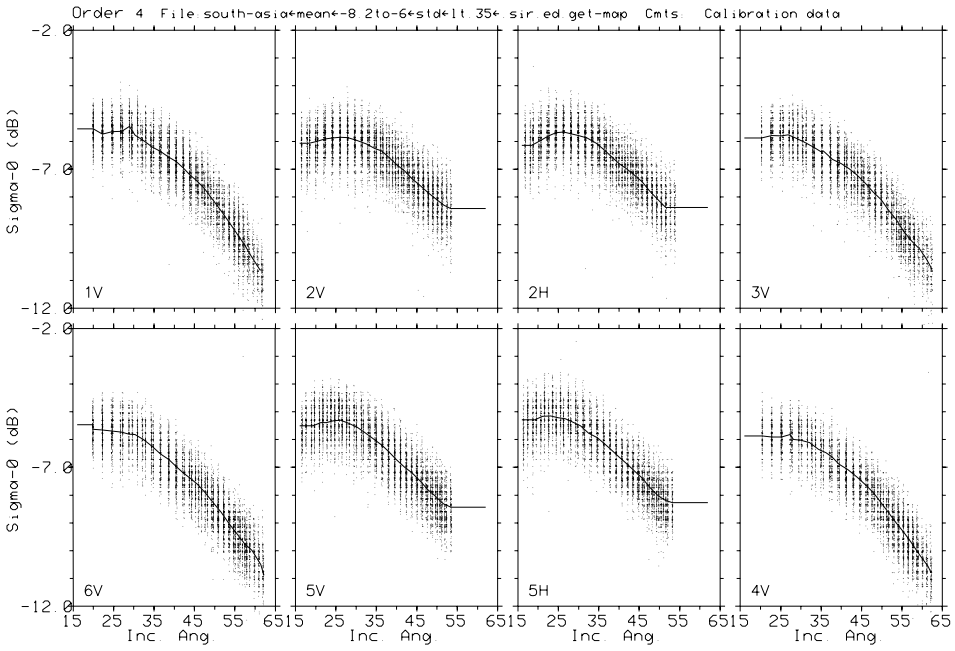

Figure 3.12: *Measured σ°_{meas} from the rainforests of southeast Asia.*

3.5 Summary

This chapter has presented criteria and methodology for selecting land surface regions for calibration of a spaceborne scatterometer. This method uses uncalibrated data to form time-series of images land surface regions using the SIRF algorithm. The time-series of images is used to form temporal mean and standard deviation images under the assumption that the instrument is relatively stable. Finally, calibration regions are determined based on common mean and standard deviation parameters on a pixel-by-pixel basis. This process was demonstrated in detail for the Amazon rainforest region which is widely considered the most useful for scatterometer calibration. Four other calibration regions were also presented. Only measurement data collected over the selected calibration regions is used in the calibration process.

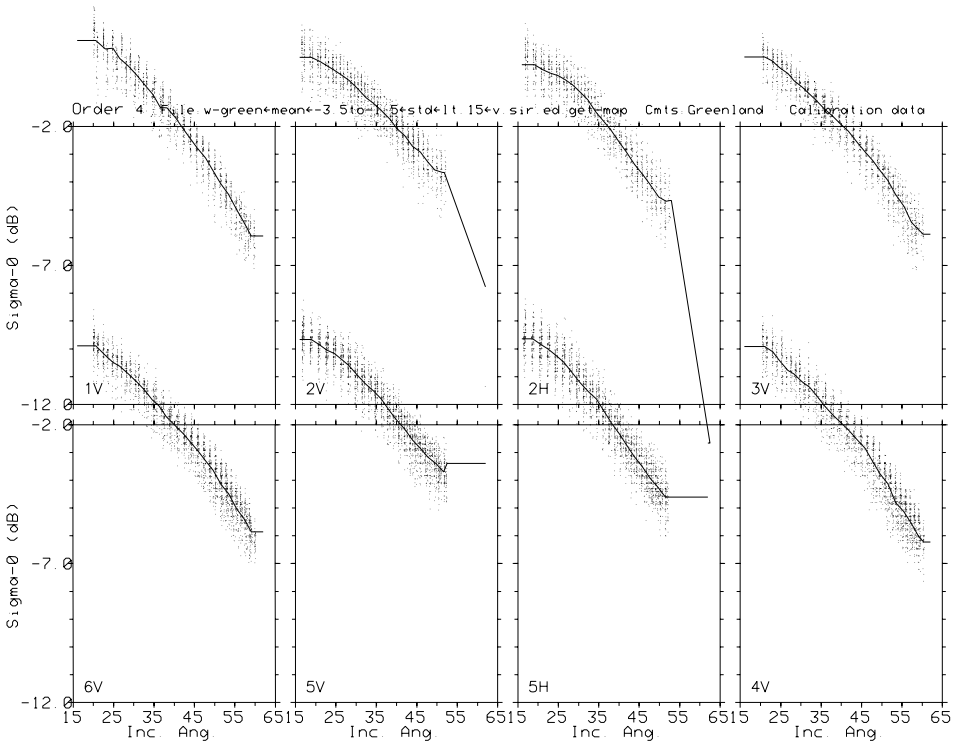

Figure 3.13: *Measured σ°_{meas} from the snow and ice layers of Greenland.*

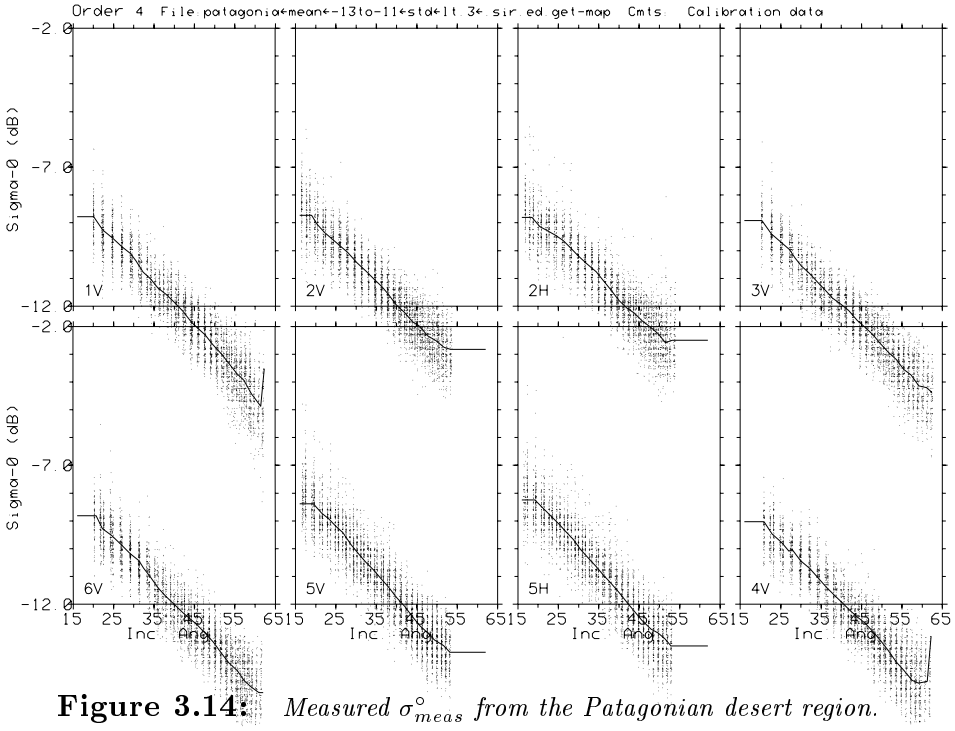

Figure 3.14: *Measured σ°_{meas} from the Patagonian desert region.*

The next chapter presents the theory of calibrating spaceborne scatterometers using land surface measurements.

Chapter 4

CALIBRATION USING LAND TARGETS

The objective of post-launch calibration is to remove σ° measurement errors due to relative biases, also known as "beam-to-beam" or "interbeam" biases. Absolute bias, which effects all beams equally, is difficult to quantify as no ground truth data or calibrated targets are available. The completed interbeam calibration is defined by a table (or set of equations) which lists the calibration correction for each beam at all incidence angles of interest. Calibration corrections thus obtained are applied to the original σ° measurement data yielding scientifically useful, *calibrated* σ° measurement data.

In the past, two sources have been used to calibrate spaceborne scatterometers: 1) ground stations, and 2) homogeneous land targets. Calibration of the Seasat-A satellite scatterometer (SASS, 1978) used land targets only [6], while the European Remote Sensing scatterometer (Escat, 1992) used both sources [7]. This thesis only uses land targets. However, other members of the NSCAT calibration/validation team use ground stations and a new technique involving σ° measurements over the ocean. Thus, several approaches have been undertaken to produce calibration corrections for NSCAT.

In this chapter, an algorithm is derived to calibrate NSCAT σ° measurement data based on measurements retrieved over designated calibration land regions. The development applies the least-squares method of Long and Skouson [3]. A discussion of the process used to designate these calibration land regions appears in the Chapter 3.

4.1 Model of σ° Response

The first step in calibrating the instrument is to develop a model of the instrument's σ° versus incidence angle (θ) response, which is also simply referred to as the "σ° response". Because NSCAT's 8 beams are independent measurement systems, each beam must be modeled independently. As described in Chapter 3, several calibration regions were selected to estimate the σ° versus incidence angle response of the different beams. Briefly, such regions were required to be free of

azimuth angle dependence, have a narrow range of σ°_{meas} values at 40° incidence angle (*i.e.*, its $\mathcal{A}$-values), exhibit little change with time in σ° at 40°, and be spatially large. This section presents a simple model that is convenient and efficient for use in calibration.

The σ° versus θ response for each beam is a function of the observation geometry, the antenna gain pattern, and the surface response. The measurements σ°_{meas} are noisy with variance $K_P^2 \sigma^{\circ\,2}_{meas}$, further complicating the problem. Following the lead of Skouson and Long [2,3], the σ°_{meas} samples are approximated by a deterministic function, $\hat{\sigma^\circ}_{meas}(\theta)$, using regression analysis. That is, $\hat{\sigma^\circ}_{meas}(\theta)$ estimates a one-to-one relationship between incidence angle (θ) and backscatter coefficient (σ°):

$$\hat{\sigma^\circ}_{meas}(\theta) \sim \sigma^\circ(\theta). \tag{4.1}$$

Using regression analysis to determine $\hat{\sigma^\circ}_{meas}(\theta)$ introduces several design issues for the regression procedure. First, what functional form (or model) should be used to construct $\hat{\sigma^\circ}_{meas}(\theta)$? Second, what order of the function is needed? Finally, what method should be used to determine the coefficients that weight the functions?

Skouson and Long [2,3] proposed use of polynomials in θ. These functions are conceptually easy to understand. The number of extrema for a polynomial is $N-1$, where N is its order. Experience from other scatterometers suggests that $\hat{\sigma^\circ}_{meas}$ is a "smooth" function of θ. Further, most calibration regions are characterized by rough surface scattering which predicts a smooth, monotonically decreasing σ° with incidence angle. Thus, a low-order polynomial is sufficient. Skouson and Long [2,3] analyzed polynomial functions of order 2 thru 5 and determined that 4^{th} order polynomial functions provide a suitable representation of the σ°_{meas} samples and estimate of $\sigma^\circ(\theta)$. Higher order polynomials add little new information. Thus, for each beam b, the σ° response is estimated by the polynomial function

$$\hat{\sigma^\circ}_{meas}(b,\theta) = c_0(b) + c_1(b)\theta + c_2(b)\theta^2 + c_3(b)\theta^3 + c_4(b)\theta^4 \tag{4.2}$$

with coefficients $c_i(b)$ to be determined for each beam.

Choosing a method to estimate the coefficients $c_i(b)$ for the polynomial functions is a matter of selecting an optimization rule. That is, based on what criterion(a) should the estimate $\hat{\sigma^\circ}_{meas}(\theta)$ be formed from the samples (measurements) σ°_{meas}? Many alternatives are possible, including least squares, weighted least squares, and minimum mean squared error. Skouson and Long [2,3] used both least

squares and weighted least squares. In this thesis, the development will assume use of least squares, though the final equations will also be presented in terms of weighted least squares. Weighted least squares is an attractive alternative to ordinary least squares because measurements obtained with greater uncertainty (variance) are "de-emphasized". This leads to an estimate of $\sigma^\circ(\theta)$ that is less dependent upon erroneous measurements. However, at the time of this work, no theoretical data was available to suggest the variance of the measurements, thus making use of weighted least squares impractical.

Each beam's σ° response must be estimated from the finite set of $\sigma^\circ_{meas}(b,\theta)$ measurements obtained by each beam at a finite number of incidence angles. Further, these σ°_{meas} are individually subject to probabilistic bias and uncertainty. The bias for each beam is assumed to be the sum of two contributing terms: absolute bias and interbeam bias. Both of these terms are considered a function of incidence angle. Absolute bias affects all beams equally. Interbeam bias results from physical differences among the 8 beams and is necessarily a function of beam (*i.e.*, the beam number). Thus, each beam's $\sigma^\circ_{meas}(\theta)$ measurements are assumed to be the sum of the *true* $\sigma^\circ(\theta)$ response, the absolute bias, and the interbeam bias. In equation form, this gives

$$\sigma^\circ_{meas}(b,\theta) = \sigma^\circ_{tr}(b,\theta) + \sigma^\circ_{abs}(b,\theta) + \sigma^\circ_{ibb}(b,\theta), \qquad b = 1,\ldots,8. \tag{4.3}$$

Because it is impossible to differentiate absolute bias and true σ°, the two terms are combined forming the *effective* σ°:

$$\sigma^\circ_{meas}(b) = \sigma^\circ_{eff}(b) + \sigma^\circ_{ibb}(b), \qquad b = 1,\ldots,8. \tag{4.4}$$

Each of the terms in Equation 4.4 are now represented using 4^{th} order polynomial functions, as in Equation 4.2, yielding

$$\begin{aligned}
\hat{\sigma^\circ}_{meas}(b,\theta) &= P_{meas}(0,b) + P_{meas}(1,b)\theta + \cdots + P_{meas}(4,b)\theta^4 \qquad (4.5)\\
\hat{\sigma^\circ}_{eff}(b,\theta) &= P_{eff}(0,b) + P_{eff}(1,b)\theta + \cdots + P_{eff}(4,b)\theta^4\\
\hat{\sigma^\circ}_{ibb}(b,\theta) &= P_{ibb}(0,b) + P_{ibb}(1,b)\theta + \cdots + P_{ibb}(4,b)\theta^4
\end{aligned}$$

where P_{meas}, P_{eff}, and P_{ibb} are the polynomial coefficients associated with $\sigma^\circ_{meas}(b)$, $\sigma^\circ_{eff}(b)$, and $\sigma^\circ_{ibb}(b)$, respectively. Equation 4.4 now becomes

$$\hat{\sigma^\circ}_{meas}(b) = \hat{\sigma^\circ}_{eff}(b) + \hat{\sigma^\circ}_{ibb}(b) + \hat{\sigma^\circ}_{err}, \qquad b = 1,\ldots,8 \tag{4.6}$$

where $\hat{\sigma^\circ}_{err}$ is the error due to equating the polynomial approximations to the functions of Equation 4.4. Combining Equations 4.5 and 4.6 and collecting coefficients of like terms obtains the following set of 40 equations:

$$\begin{aligned} P_{meas}(c,b) &= P_{eff}(c,b) + P_{ibb}(c,b) + P_{err}(c,b), \\ & \qquad c = 0, \ldots, 4 \\ & \qquad b = 1, \ldots, 8. \end{aligned} \tag{4.7}$$

These equations form the model of the σ° response of the instrument. In order to proceed, some reasonable assumptions must be made on the functions in Equation 4.4 and extend the assumption to the associated coefficients in Equations 4.5 and 4.7. For any Earth location, the $P_{eff}(c,b)$ are assumed constant for all beams at a point in time. For areas (such as calibration land regions) that exhibit little σ° change over a given time period, $P_{eff}(c,b)$ are assumed constant over that time period. The $P_{ibb}(c,b)$ are assumed constant over the entire Earth (though necessarily different for each beam) for "long" periods of time (longer than the data set). The P_{err} are unknown, but assumed to be small based on Skouson's evaluation [2]. With the σ° response modeled, the technique may now be developed for estimating the interbeam bias, σ°_{ibb}.

4.2 Derivation of Estimation Algorithm

The estimated interbeam bias function, $\hat{\sigma^\circ}_{ibb}$, and its associated coefficients, $P_{ibb}(c,b)$, are only properly defined with respect to a reference beam. The reference beam's $\hat{\sigma^\circ}_{meas}$ is defined to be "correct". This thesis uses beam 7, or antenna 3V, as the reference beam in accordance with instructions from the NSCAT calibration/validation team. Thus, $P_{ibb}(c,7) \equiv 0$ for $c = 0, \ldots, 4$. Subtracting Equation 4.7 with $b = 7$ from itself for all other b gives

$$P_{meas}(c,b) - P_{meas}(c,7) = P_{ibb}(c,b) + P_{err}(c,b) - P_{err}(c,7) \tag{4.8}$$

or

$$\begin{aligned} \Delta P_{meas}(c,b) &= P_{ibb}(c,b) + \Delta P_{err}(c,b) \\ & \qquad b = 1, \ldots, 6, 8. \end{aligned} \tag{4.9}$$

Because the P_{err} are assumed to be small, $\Delta P_{err}(c,b) \approx 0$ leaves

$$\begin{aligned} P_{ibb}(c,b) &\approx \Delta P_{meas}(c,b), \\ & \qquad b = 1, \ldots, 6, 8. \end{aligned} \tag{4.10}$$

Thus, to obtain an estimate of the interbeam bias, $\hat{\sigma^\circ}_{ibb}$ (again, assumed constant over calibration regions), coefficients $P_{meas}(c,b)$ must be found that estimate $\hat{\sigma^\circ}_{meas}$ over the calibration regions for each beam. By then forming $\Delta P_{meas}(c,b)$, an estimate of the interbeam bias function, $\hat{\sigma^\circ}_{ibb}(\theta)$, is given according to Equations 4.10 and 4.5. Calibration of NSCAT measurement data is then done by removing $\hat{\sigma^\circ}_{ibb}(\theta = \theta_{meas})$ from the original $\sigma^\circ_{meas}(\theta)$ measurements. Coefficients $P_{meas}(c,b)$ are thus sought that minimize the error in approximating $\sigma^\circ_{meas}(\theta)$ with $\hat{\sigma^\circ}_{meas}(\theta)$. This leads naturally to the use of least squares estimation.

4.2.1 Least Squares Formulation

The error in approximating $\sigma^\circ_{meas}(\theta)$ with $\hat{\sigma^\circ}_{meas}(\theta)$ may be minimized in the least-square sense by realizing that the same P_{meas} coefficients must be used for all σ° measurements from a calibration region (for a given beam). Equation 4.5 may be transformed into a matrix equation and written as

$$\overline{\sigma^\circ}_{meas}(b) = \Theta \bar{P}_{meas}(b) \tag{4.11}$$

where

$$\begin{aligned} \overline{\sigma^\circ}_{meas}(b) &= [\sigma^\circ_1(b,\theta_1) \cdots \sigma^\circ_N(b,\theta_N)]^{\mathbf{T}}, \\ \Theta &= \begin{bmatrix} 1 & \theta_1(b) & \theta_1(b)^2 & \theta_1(b)^3 & \theta_1(b)^4 \\ 1 & \theta_2(b) & \theta_2(b)^2 & \theta_2(b)^3 & \theta_2(b)^4 \\ \vdots & \vdots & \vdots & \vdots & \vdots \\ 1 & \theta_N(b) & \theta_N(b)^2 & \theta_N(b)^3 & \theta_N(b)^4 \end{bmatrix} \end{aligned}$$

and,

$$\begin{aligned} \bar{P}_{meas}(b) &= [P_{meas}(0,b) \cdots P_{meas}(4,b)]^{\mathbf{T}} \\ b &= 1, \ldots, 8 \end{aligned}$$

where N is the number of measurements available for beam b.

To obtain the least squares estimate of $\bar{P}_{meas}(b)$ in Equation 4.11, the Penrose-Moore pseudo-inverse of Θ, $\Theta^\dagger = (\Theta^{\mathbf{T}}\Theta)^{-1}\Theta^{\mathbf{T}}$, is used to obtain

$$\hat{\bar{P}}_{meas}(b) = \Theta^\dagger \overline{\sigma^\circ}_{meas}(b). \tag{4.12}$$

Using weighted least squares, the pseudo-inverse is given by

$$\Theta^{\dagger} = (\Theta^{\mathbf{T}}\mathbf{R}^{-\mathbf{1}}\Theta)^{-1}\Theta^{\mathbf{T}}\mathbf{R}^{-\mathbf{1}},$$

where

$$\begin{aligned}\mathbf{R} &= E[\overline{\sigma^{\circ}}_{meas}(b)^{\mathbf{T}} \cdot \overline{\sigma^{\circ}}_{meas}(b)] \\ &= \begin{bmatrix} K_{P_1}^2 & 0 & \cdots & 0 \\ 0 & K_{P_2}^2 & \cdots & 0 \\ \vdots & \ddots & \ddots & \vdots \\ 0 & \cdots & 0 & K_{P_N}^2 \end{bmatrix}\end{aligned} \tag{4.13}$$

K_P^2, as mentioned earlier, is the normalized variance of the measurement error. K_P^2 is a useful weighting function because it is the normalized variance of $\sigma^{\circ}_{meas}(\theta)$. Using the variance of $\sigma^{\circ}_{meas}(\theta)$, which is given by $K_P^2\sigma^{\circ\,2}_{meas}(\theta)$, would lead to a non-linear system, so K_P^2 alone is used. Equation 4.12 may be interpreted as using $\mathbf{R} = \mathbf{I}$ to weight the measurements.

Equations 4.11 thru 4.12, as written, are valid for a single calibration region. Each individual region's $\hat{\sigma^{\circ}}_{meas}$ and P_{meas} must be formed independently using the measurements of that region. Additionally, measurements for each region are obtained at two different times during the day (corresponding to the ascending and descending passes) and because these two different times are approximately 11–13 hours apart, it is prudent to assume that the effective σ° response, $\sigma^{\circ}_{eff}(\theta)$, and the associated coefficients, $P_{eff}(c,b)$, are significantly different for ascending and descending passes. Thus, Equations 4.11 thru 4.12 should be formed and calculated independently for measurement data from both ascending and descending passes over every calibration region. The resulting $P_{meas}(c,b)$ are then used in Equation 4.10 to obtain the interbeam bias.

4.3 Summary

This chapter has presented the technique of Long and Skouson for estimating the interbeam bias using calibration regions and measurement data [2, 3]. It is based on a number of reasonable assumptions that lead to a least-squares formulation (with potential for extending to weighted least squares). The next chapter extends the technique to estimate the interbeam bias and the spacecraft's attitude error simultaneously.

Chapter 5

ESTIMATING ADEOS ATTITUDE USING NSCAT MEASUREMENTS

During the initial months of NSCAT's mission, the attitude sensors onboard the ADEOS spacecraft (host of the NSCAT instrument) were determined to be inaccurate. Erroneous attitude information was being used to calculate σ°. The resulting σ° values thus contained biases. In addition to calibrating the instrument's interbeam biases, the bias due to attitude errors must also be removed. This chapter extends the technique of the previous chapter to simultaneously estimate the spacecraft's attitude errors and the instrument's interbeam biases. Results of applying this technique to actual NSCAT data and variations of the technique are presented in the following chapter.

5.1 Bias Introduced in σ° by Attitude Error

To understand why erroneous spacecraft attitude information introduces a bias in σ°, consider the radar equation:

$$\sigma^\circ = \frac{(4\pi)^3 R^4 G_p P_r}{\lambda^2 L_s G^2 A_C P_t} \tag{5.1}$$

where R is the slant range to the observed ground area, G_p is the processor gain, P_r is the power received, λ is the wavelength of the carrier frequency, L_s is the system loss, G is the antenna gain (transmit and receive), A_C is the area of the ground observed in the current Doppler cell, and P_t is the power transmitted. When the radar's attitude is not accurate, the geometry between the radar and the ground is directly affected. Thus, in the radar equation, R and A_C, the range to the measured surface and its area, are incorrect.

Fortunately, it is possible to calculate the value of R and A_C for many different spacecraft attitudes. These values may then be applied in the radar equation to produce new σ° values. σ° is thus a function of the spacecraft attitude (roll, pitch, and yaw). In NSCAT's case, because the reported attitude is considered erroneous, the calculated σ° becomes a function of attitude *error*. In effect, the attitude error introduces a bias (in dB space) in the measured σ°_{meas} denoted by σ°_{att}. Further,

because all 6 antenna (or 8 beams) are on the same spacecraft, all suffer from the same attitude angle errors (designated e_r, e_p, and e_y for roll, pitch, and yaw error, respectively). Note, however, that each antenna is oriented differently and thus the roll, pitch, and yaw error affect each antenna's geometry to the ground differently. The σ°_{att} applied to σ° is thus a function of not only attitude error, but also of antenna (or beam) number: $\sigma^\circ_{att}(e_r, e_p, e_y, b)$.

Vincent Hsiao, of the Jet Propulsion Laboratory, produced a table of $\sigma^\circ_{att}(e_r, e_p, e_y, b)$ correction values to be added to the original calculated σ° in order to compensate for attitude errors in roll, pitch, and yaw for each beam, respectively [17]. Hsiao's table provides corrections for attitude errors ranging from -1.6° to 1.6° in increments of 0.2° in each dimension. Thus, if the spacecraft's correct attitude can be estimated, Hsiao's table can be utilized to remove the attitude error bias σ°_{att} from the calculated σ°.

5.2 Estimating Attitude Error σ°_{att}

The calibration technique of the previous chapter proved remarkably adaptable for the purpose of estimating σ°_{att} (and thus the corresponding attitude errors e_r, e_p, e_y). This section presents the derivation of a method for *simultaneously* estimating the attitude errors and the interbeam bias corrections, σ°_{ibb}.

Equations 4.4-4.7 are expanded to include the attitude error bias as follows:

$$\sigma^\circ_{meas}(b) = \sigma^\circ_{eff} + \sigma^\circ_{ibb} + \sigma^\circ_{att} \tag{5.2}$$

$$\sigma^\circ_{meas} \approx \hat{\sigma^\circ}_{meas}(b) = \hat{\sigma^\circ}_{eff} + \hat{\sigma^\circ}_{ibb} + \hat{\sigma^\circ}_{att} + \hat{\sigma^\circ}_{err} \tag{5.3}$$

$$P_{meas}(c,b) = P_{eff}(c,b) + P_{ibb}(c,b) + P_{att}(c,b) + P_{err}(c,b) \tag{5.4}$$

$$c = 1, \ldots, 4$$

$$b = 1, \ldots, 8$$

where σ°_{meas} is the measured σ°, σ°_{eff} is the effective true σ°, σ°_{ibb} is the interbeam bias, and σ°_{att} is the attitude bias. In Equation 5.4, $P_{meas}(c,b)$ are given by Equations 4.11 and 4.12. For a given calibration region, P_{eff} is assumed constant for all beams over the entire data set. P_{ibb} is assumed constant for all calibration regions over the duration of the data set (though necessarily different for each beam). P_{att} is assumed to be different for each beam and possibly varying with respect to latitude for both ascending and descending passes. P_{err} is unknown, but is assumed to be small as in Chapter 4.

5.2.1 Modeling and Approximations

As mentioned earlier, the interbeam bias, P_{ibb}, is only properly defined with respect to a reference and beam 7, or antenna 3V, was used as the reference; thus, $P_{ibb}(c,7) = 0$ for all coefficients. Following the same procedure as in Chapter 4, Equation 5.4 is subtracted with $b = 7$ from itself for all other b, yielding

$$\begin{aligned} P_{meas}(c,b) - P_{meas}(c,7) &= P_{ibb}(c,b) + (P_{att}(c,b) - P_{att}(c,7)) + \\ &\quad (P_{err}(c,b) - P_{err}(c,7)) \end{aligned} \tag{5.5}$$

or,

$$\begin{aligned} \Delta P_{meas}(c,b) &= P_{ibb}(c,b) + \Delta P_{att}(c,b) + \Delta P_{err}(c,b) \\ &\qquad b = 1, \ldots, 6, 8. \end{aligned} \tag{5.6}$$

P_{err} is assumed to be small with $\Delta P_{err}(c,b) \approx 0$, leaving

$$\begin{aligned} \Delta P_{meas}(c,b) &\approx P_{ibb}(c,b) + \Delta P_{att}(c,b), \\ &\qquad b = 1, \ldots, 6, 8. \end{aligned} \tag{5.7}$$

5.2.2 Finding $\Delta P_{att}(c,b)$

Denote the roll, pitch, and yaw errors by $e_r, e_p,$ and e_y (in units of degrees[$^\circ$]) and the corresponding biases added to σ°_{eff} by $\sigma^\circ_r, \sigma^\circ_p,$ and σ°_y. As a convenient simplification, treat each of the attitude biases as dependent only upon its respective attitude dimension:

$$\begin{aligned} \sigma^\circ_r &= f_r(e_r), \\ \sigma^\circ_p &= f_p(e_p), \end{aligned} \tag{5.8}$$

and,

$$\sigma^\circ_y = f_y(e_y).$$

The total attitude bias correction for each beam, $\sigma^\circ_{att}(c,b)$ is assumed to be linearly dependent on $\sigma^\circ_r, \sigma^\circ_p,$ and σ°_y; that is,

$$\sigma^\circ_{att} = \sigma^\circ_r + \sigma^\circ_p + \sigma^\circ_y. \tag{5.9}$$

This simplification implicitly assumes a small angle approximation for each of the attitude angle errors. Attitude angle errors are expected to be less than 1° which

justifies this approximation. Combining the previous two equations, the total attitude bias is a function of the attitude errors, given by

$$\sigma^{\circ}_{att} \quad = \quad f_r(e_r) + f_p(e_p) + f_y(e_y). \tag{5.10}$$

Now, making a similar polynomial approximation for each of the attitude bias functions yields

$$P_{att}(c,b) = P_r(e_r,c,b) + P_p(e_p,c,b) + P_y(e_y,c,b). \tag{5.11}$$

Attitude bias correction data was calculated by Vincent Hsaio as a function of incidence angle (the reported incidence angle; that is, not corrected for attitude errors). The relationship between attitude bias and incidence angle is nonlinear. Figures 5.1 , 5.2, and 5.3 are examples of the correction data for Beam 1 Roll, Pitch, and Yaw for latitudes near the Equator. The data are separated between ascending and descending passes because the measurement geometry is different. The actual data points provided by Hsaio are indicated by dots. The lines are 4^{th}-order least-squares fits to the data corresponding to attitude errors of -1.6° to 1.6° in increments of 0.2°.

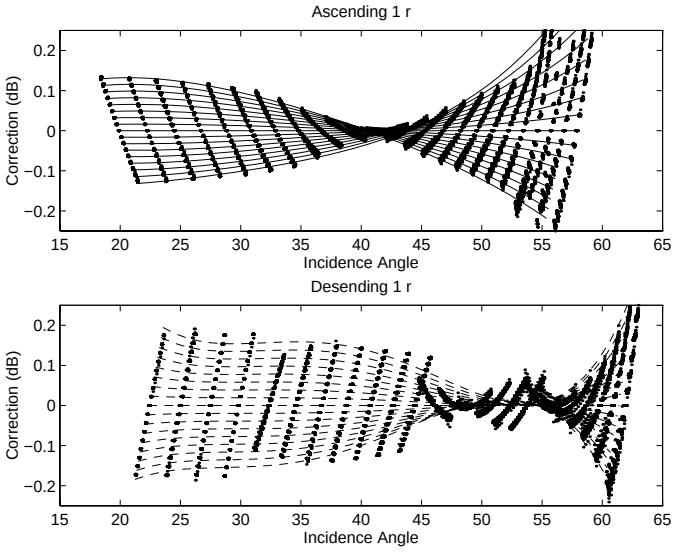

Figure 5.1: *Attitude bias correction versus reported incidence angle for Beam 1 Roll Error for latitudes near the Equator (separated for ascending and descending passes). Hsaio's data points are indicated by dots while 4^{th}-order fits to these data are shown with lines. Each line attempts to fit data corresponding to roll errors quantized in 0.2° increments. In this example, the ascending passes' fits are good while the descending passes' fits are poor.*

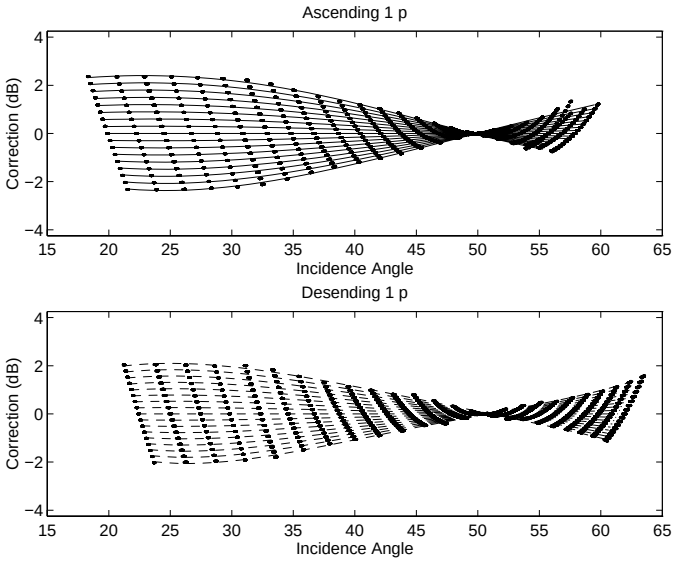

Figure 5.2: *Attitude bias correction versus reported incidence angle for Beam 1 Pitch Error (separated for ascending and descending passes). Hsaio's data points are indicated by dots while 4^{th}-order fits to these data are shown with lines. Each line attempts to fit data corresponding to pitch errors quantized in $0.2°$ increments.*

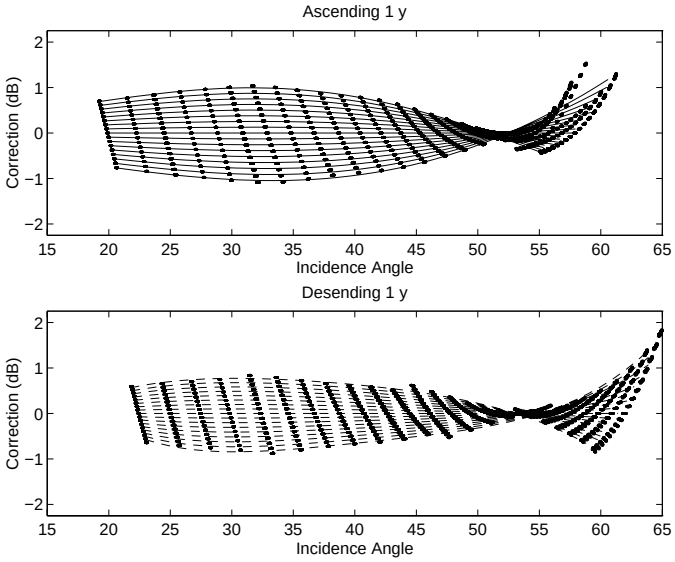

Figure 5.3: *Attitude bias correction versus reported incidence angle for Beam 1 Yaw Error (separated for ascending and descending passes). Hsaio's data points are indicated by dots while 4^{th}-order fits to these data are shown with lines. Each line attempts to fit data corresponding to yaw errors quantized in $0.2°$ increments.*

The coefficients of the least-square fits to the attitude bias versus incidence angle curves are then grouped by coefficient number (0-4), beam (1-8), attitude error

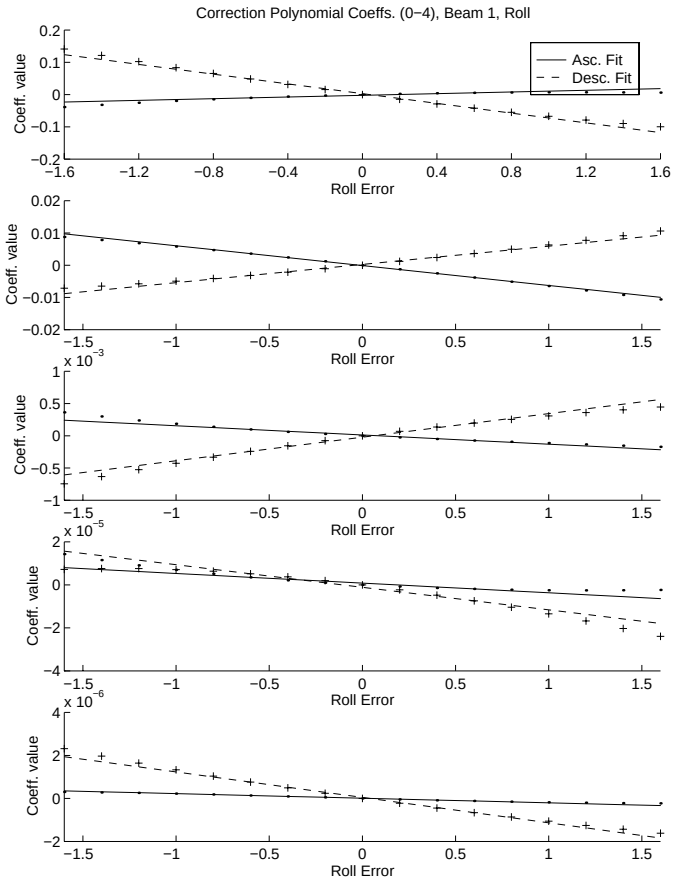

Figure 5.4: *Polynomial coefficients resulting from 4^{th}-order fits to attitude correction data of Figure 5.1 plotted versus roll error for Beam 1. Linear fit approximations to these polynomial coefficients are also plotted. The polynomials appear to be well-represented by linear approximations, in general.*

type (roll, pitch, or yaw), and ascending or descending pass. These grouped coefficients are plotted versus attitude error. The coefficient plots for Beam 1 Roll error near the equator are found in Figure 5.4. A *linear* approximation is also included. The polynomial coefficients are generally linear versus attitude error and pass through the origin. Thus, the slope of the linear approximations may be used to map attitude error to the corresponding attitude bias correction polynomial coefficients. That is,

$$\begin{aligned} P_r(e_r, c, b) &= m_r(c, b) \cdot e_r, \\ P_p(e_p, c, b) &= m_p(c, b) \cdot e_p, \end{aligned}$$

and,

$$P_y(e_y, c, b) = m_y(c, b) \cdot e_y$$

where $m_r(c,b)$, $m_p(c,b)$, and $m_y(c,b)$ represent the slope of the linear approximation of the attitude error versus attitude correction coefficient values. Equation 5.11 becomes:

$$P_{att}(c,b) = m_r(c,b)\cdot e_r + m_p(c,b)\cdot e_p + m_y(c,b)\cdot e_y.$$

Normalizing to beam 7, ΔP_{att} may now be written:

$$\begin{aligned}\Delta P_{att}(c,b) &= \Delta m_r(c,b)\cdot e_r + \Delta m_p(c,b)\cdot e_p + \\ &\quad \Delta m_y(c,b)\cdot e_y,\end{aligned} \tag{5.12}$$

where

$$\begin{aligned}\Delta m_r(c,b) &= m_r(c,b) - m_r(c,7)\\ \Delta m_p(c,b) &= m_p(c,b) - m_p(c,7)\\ \Delta m_y(c,b) &= m_y(c,b) - m_y(c,7).\end{aligned}$$

Inserting Equation 5.12 into 5.7, finally yields

$$\begin{aligned}\Delta P_{meas}(c,b) \approx\ & P_{ibb}(c,b) + \Delta m_r(c,b)\cdot e_r + \Delta m_p(c,b)\cdot e_p + \\ & \Delta m_y(c,b)\cdot e_y \\ & c = 0,\ldots,4 \\ & b = 1,\ldots,6,8.\end{aligned} \tag{5.13}$$

The unknowns in this system of 35 equations are the interbeam biases, $P_{ibb}(c,b)$, and the attitude errors (e_r, e_p, and e_y). The attitude errors will be constant for all coefficients c and beams b. There are, therefore, 38 unknowns and Equation 5.13 is underdetermined. Estimation of the unknowns in underdetermined systems may be accomplished with the method of least squares.

5.2.3 Least Squares Formulation

The matrix equation equivalent of equation 5.13 is given by

$$\overline{\Delta P_{meas}} = \mathbf{M}\bar{B} \tag{5.14}$$

where

$$\begin{aligned}\overline{\Delta P_{meas}} &= [\Delta P_{meas}(0,1)\ \cdots\ \Delta P_{meas}(0,6)\ \Delta P_{meas}(0,8)\ \cdots \\ &\quad \cdots\ \Delta P_{meas}(4,1)\ \cdots\ \Delta P_{meas}(4,6)\ \Delta P_{meas}(4,8)]^{\mathbf{T}},\end{aligned} \tag{5.15}$$

$$\begin{aligned}\bar{B} &= [P_{ibb}(0,1)\ \cdots\ P_{ibb}(0,6)\ P_{ibb}(0,8)\ \cdots \\ &\quad \cdots\ P_{ibb}(4,1)\ \cdots\ P_{ibb}(4,6)\ P_{ibb}(4,8)\ e_r\ e_p\ e_y]^{\mathbf{T}}\end{aligned} \tag{5.16}$$

and,

$$\mathbf{M} = \begin{bmatrix} \mathbf{I}_7 & \mathbf{0}_7 & \mathbf{0}_7 & \mathbf{0}_7 & \mathbf{0}_7 & \Delta m_r(0,1) & \Delta m_p(0,1) & \Delta m_y(0,1) \\ & & & & & \vdots & \vdots & \vdots \\ & & & & & \Delta m_r(0,6) & \Delta m_p(0,6) & \Delta m_y(0,6) \\ & & & & & \Delta m_r(0,8) & \Delta m_p(0,8) & \Delta m_y(0,8) \\ \mathbf{0}_7 & \mathbf{I}_7 & \mathbf{0}_7 & \mathbf{0}_7 & \mathbf{0}_7 & \vdots & \vdots & \vdots \\ \mathbf{0}_7 & \mathbf{0}_7 & \mathbf{I}_7 & \mathbf{0}_7 & \mathbf{0}_7 & \vdots & \vdots & \vdots \\ \mathbf{0}_7 & \mathbf{0}_7 & \mathbf{0}_7 & \mathbf{I}_7 & \mathbf{0}_7 & \vdots & \vdots & \vdots \\ \mathbf{0}_7 & \mathbf{0}_7 & \mathbf{0}_7 & \mathbf{0}_7 & \mathbf{I}_7 & \Delta m_r(4,1) & \Delta m_p(4,1) & \Delta m_y(4,1) \\ & & & & & \vdots & \vdots & \vdots \\ & & & & & \Delta m_r(4,6) & \Delta m_p(4,6) & \Delta m_y(4,6) \\ & & & & & \Delta m_r(4,8) & \Delta m_p(4,8) & \Delta m_y(4,8) \end{bmatrix}. \quad (5.17)$$

To obtain the ordinary least squares estimate of $\bar{B}$ in Equation 5.14, the Penrose-Moore pseudoinverse of $\mathbf{M}$, $\mathbf{M}^\dagger$, is used to obtain

$$\hat{\bar{B}} = \mathbf{M}^\dagger \overline{\Delta P_{meas}} \quad (5.18)$$

where

$$\mathbf{M}^\dagger = (\mathbf{M}^\mathbf{T}\mathbf{M})^{-1}\mathbf{M}^\mathbf{T}. \quad (5.19)$$

The interbeam biases, as previously stated, are assumed to be constant over all regions. The $\Delta m_{r,p,y}(c,b)$ are specific to latitude bands and are different for ascending and descending passes. Hsaio's data is separated into three bands: $-53°$ to $-35°$, $-10°$ to $5°$, and $-62°$ to $72°$. Equations 5.14 thru 5.18, as written, are valid for one region and only for the ascending or descending pass. Fortunately, they may easily be expanded to allow both ascending and descending passes, multiple regions from the same latitude band, and multiple latitude bands.

In Chapter 4, weighted least squares was proposed as an alternative method to determine the $P_{meas}(c,b)$ coefficients. That may again be used here (if K_P are available for the measurement $\sigma^\circ_{meas}(\theta)$). However, to extend weighted least squares to Equation 5.19, some knowledge of the quality of the $P_{meas}(c,b)$ coefficients must be obtained. Such a measure of $P_{meas}(c,b)$ quality would be used to populate the $\mathbf{R}$ weighting matrix. For simplicity in this work, weighted least squares is not used.

5.2.4 Expanding to Multiple Regions

Expanding Equations 5.14–5.17 to allow multiple regions, latitude bands, and/or ascending and descending passes is a matter of carefully and systematically reorganizing and expanding $\overline{\Delta P_{meas}}$, $\mathbf{M}$, and, $\bar{B}$.

$\overline{\Delta P_{meas}}$ is not difficult:

$$\overline{\Delta P_{meas}} \;=\; [\overline{\Delta P_{meas}}(Region\ 1)\cdots\overline{\Delta P_{meas}}(Region\ N)]^{\mathbf{T}}. \tag{5.20}$$

$\bar{B}$ is somewhat more involved. While no additional $P_{ibb}(c,b)$ elements are needed (because the interbeam bias is constant for all regions, ascending and descending), another set of $e_r, e_p,$ and e_y elements must be appended for each new latitude band, ascending or descending. If Region 1 and Region 2 are from different latitude bands,

$$\begin{aligned}\bar{B} \;=\; & [P_{ibb}(0,1)\cdots P_{ibb}(0,6)\ P_{ibb}(0,8)\cdots \\ & \cdots P_{ibb}(4,1)\cdots P_{ibb}(4,6)\ P_{ibb}(4,8) \\ & e_{r,asc}(R1)\ e_{p,asc}(R1)\ e_{y,asc}(R1)\ e_{r,desc}(R1)\ e_{p,desc}(R1)\ e_{y,desc}(R1) \\ & e_{r,asc}(R2)\ e_{p,asc}(R2)\ e_{y,asc}(R2)\ e_{r,desc}(R2)\ e_{p,desc}(R2)\ e_{y,desc}(R2)]^{\mathbf{T}}.\end{aligned} \tag{5.21}$$

However, if a Region 3 is to also be included, but it is from the same latitude band as Region 1 or 2, then no new attitude error elements need be added.

$\mathbf{M}$ is complicated to organize. Each new region (ascending and descending) is represented by a new set of rows, similar in structure to the others. The leading columns of identity and zeros matrices must be identically repeated in every case. The next series of columns contain the "slope" elements. If the new region is from the same latitude band and in the same pass direction (ascending or descending) as another region, the other region's slope elements must be repeated here. If the new region is from a different latitude band or is for a different pass direction, zero matrices must be included below all other regions' slope elements and the new region's slope elements must be appended in new columns. Zero matrices must be appended to the other regions' rows in these new columns. By following these rules, as many latitude bands' attitude errors as desired (ascending and descending) may be estimated.

5.3 Summary

This chapter has extended the method of Long and Skouson [2, 3] for the calibration of spaceborne scatterometers to simultaneously estimate spacecraft attitude error. This extension relies on a set of attitude correction data tabulated by Hsaio [17] for NSCAT. By making a series of reasonable assumptions, a linear relationship was found between the attitude errors (e_r, e_p, and e_y) and the attitude bias correction coefficients, $P_{att}(c, b)$. Because the system of equations thus formed is underdetermined, the method of least-squares is employed to estimate the attitude error and the calibration coefficients. With this theoretical development in place, the next step is to implement the technique on actual NSCAT measurement data.

Chapter 6

CALIBRATION AND ATTITUDE ERROR ESTIMATION RESULTS

In this chapter, the technique derived in the previous chapter is applied for simultaneously estimating interbeam biases (σ°_{ibb} or P_{ibb}) and attitude error corrections (e_r, e_p, and e_y). The goal is to find calibration corrections that yield consistent backscatter response (σ°_{eff}) for all beams. As will be seen, the underlying assumptions of the previous chapter lead to reasonable calibration and attitude error estimates, though they are not completely satisfactory. The same basic technique is also applied using slightly different underlying assumptions in an attempt to better understand the strengths and weaknesses of this technique. The results obtained from such variations are also presented.

6.1 Data Sets and Calibration Regions

Several sets of raw NSCAT data from different time periods are used as inputs to the algorithm. All of the data are categorized by the NSCAT Software Interface Specification [18] data standards as "L15" (Level 1.5) which contains σ°_{meas}, θ (incidence angle), and ground location data. All of these parameters are necessary for this evaluation. However, the processing that occurred before L15 (*i.e.*, Levels 0.0 and 1.0) differs for some of the data sets and is worthy of note. The most significant pre-processing difference was a result of the early "guesses" of the ADEOS spacecraft's attitude error by its Japanese flight controllers. Table 6.1 provides a summary description of the data sets.

Table 6.1: *NSCAT L1.5 Data Sets used in the Calibration/Attitude Error Estimation Analysis.*

Data Set Name	Time Period	Pre-processing Attributes
JD 269-278	JD 269-278	none
JD 279-288	JD 279-288	none
S4-S5	JD 269-282	-0.22° Yaw
JD 319-328	JD 319-328	none
S18-S19	JD 001-014	$+0.10^{\circ}$ Yaw

"JD 269-278" and "JD 279-288" are original data for the given days ("JD" abbreviates "Julian Day" which is the number of the day of the year). "S4-S5" is data reprocessed (includes Japanese attitude correction guess of -0.22° yaw) for Julian Days 269 thru 282. Because of their overlapping time periods, it is anticipated that these three data sets will yield correlated results. "JD 319-328" is original data for the given days. "S18-S19" is data reprocessed with Japanese attitude correction guess $+0.1^\circ$ yaw for Julian Days 1 thru 14 of 1997. While "S18-S19" and "JD 319-328" do not overlap (they are about 47 days apart), "JD 319-328" is the last of the original data which does not include the Japanese attitude bias assumption. Further, the Japanese suggest that the yaw bias for "JD 319-328" should also be $+0.1^\circ$.

As discussed in Chapter 3, areas from the Earth with small difference in σ° versus θ (incidence angle) response over large areas and long periods of time are suitable for the calibration technique of this paper. The five areas identified in that chapter as best meeting requirements are the Amazon rainforest region, Patagonia, the ice sheets of Western Greenland, the Congo rainforest region, and the Indonesian rainforest region. All five regions are used in this analysis toward obtaining NSCAT calibration bias corrections and ADEOS attitude error estimates.

The rainforest regions (Amazon, Congo, and Indonesia) are grouped in a single latitude band (bounded by the 10^{th} South and 5^{th} North Parallels) which is refered to as the "Equatorial Band". The other two regions, Western Greenland and Patagonia, are in two other latitude bands. The "Greenland Band" is bounded by the 62^{nd} and 72^{nd} North Parallels. The "Patagonian" band is bounded by the 35^{th} and 53^{rd} South Parallels. The three latitude bands are used to extract data from Hsaio's tables [17] to form functions of the P_{att} bias coefficients versus attitude error (e_r, e_p, and e_y) as given in Equations 5.12 and 5.12). Thus, the three Equatorial regions use the same set of attitude correction information, while Greenland and Patagonia each use another set.

6.2 Results for Primary Technique

The primary technique to estimate the attitude errors is summarized by Equations 5.14 thru 5.19. The expansions mentioned in Subsection 5.2.4 produce independent attitude error estimates of multiple latitude bands for ascending and descending passes. The corresponding interbeam bias estimate, on the other hand, is constant for all latitude bands and for both ascending and descending passes. Table

6.2 lists the attitudes estimated with this technique for several data sets. Attitude errors for Patagonia, Equatorial regions, and Western Greenland are listed.

Table 6.2: *Attitude errors estimated assuming a constant interbeam bias for Patagonia, Equatorial regions, and Western Greenland.*

Data Set	Axis	Patagonia			Equatorial			Greenland		
		Asc	Desc	Δ_{a-d}	Asc	Desc	Δ_{a-d}	Asc	Desc	Δ_{a-d}
S4-S5	R	1.17	-3.36	4.53	1.34	1.11	.24	2.54	2.24	.29
	P	.04	-.07	.11	-.09	.18	-.27	-.02	.10	-.12
	Y	1.38	1.19	.19	1.46	1.26	.20	1.73	1.45	.28
JD 269-278	R	.23	-1.70	1.93	.81	1.23	-.42	1.10	1.44	-.34
	P	-.04	-.15	.11	-.21	.04	-.25	-.16	-.01	-.15
	Y	.76	.56	.20	.79	.61	.18	1.07	.89	.18
JD 279-288	R	-.07	-4.52	4.45	.28	-.47	.75	2.46	1.25	1.21
	P	.22	.03	.18	.11	.23	-.12	.08	.29	-.21
	Y	.87	.85	.02	.98	.80	.18	1.27	1.11	.16
S18-S19	R	-1.39	-4.72	3.33	-.57	-.25	-.32	2.15	1.15	1.00
	P	.19	-.03	.22	.11	.09	.02	-.08	.14	-.22
	Y	-.40	-.53	.13	-.34	-.50	.16	.02	-.24	.26
JD 319-328	R	-.98	6.58	5.60	-0.19	-1.26	1.07	2.02	1.11	.91
	P	.85	.58	.27	.82	.72	.10	.72	.86	-.14
	Y	-.07	-.20	.13	-.02	-.13	.15	.26	.10	.16

Table 6.3: *Difference between attitude errors of different data sets listed in Table 6.2.*

Data Set	Axis	Patagonia		Equatorial		Greenland	
		Asc	Desc	Asc	Desc	Asc	Desc
JD 319-328	P	.89	.73	1.03	.68	.88	.87
- JD 269-278	Y	-.83	-.76	-.81	-.74	-.81	-.79
S18-S19	P	.15	.04	.20	-.09	-.06	.04
- S4-S5	Y	-1.78	-1.72	-1.80	-1.76	-1.71	-1.69
JD 269-278	P	-.08	-.08	-.12	-.14	-.14	-.11
- S4-S5	Y	-.62	-.63	-.67	-.65	-.66	-.56

Perhaps the first observation to make from Table 6.2 is that most of the attitude error values for the latitude bands are not consistent from one data set to the next. While the attitude is likely to be slowly time-varying, it probably should not be this erratic, especially for data sets from consecutive or overlapping time periods (*i.e.*,"S4-S5", "JD 269-278", and "JD 279-288"). However, the difference in attitude error (pitch and yaw) for several of these data sets is listed in Table 6.3. There, the

difference between data sets (especially in yaw error) is consistent for all three latitude bands, ascending and descending passes. Also included in Table 6.2 is a column Δ_{a-d} in each latitude band which is the difference in the ascending and descending passes' attitude errors, that is, $e_{r,asc} - e_{r,desc}$. In both of these "difference" measures, several interesting trends appear. These will be discussed.

A second observation from Table 6.2 is that most of the roll error estimates, e_r, are extremely large ($> 1°$). Roll errors of this size are not considered plausible. Figures 5.1, 5.2, and 5.3 reveal that the magnitude of the correction due to roll error, σ_r°, is much smaller (one or two orders of magnitude) than that due to pitch and yaw error, σ_p° and σ_y°. Hypothesizing that roll error is being used, in effect, as a "tweaking" factor in the least squares algorithm, the roll error is set to zero, and the yaw and pitch errors are recalculated. The results are presented in Table 6.4. Again, while the attitude error values do not display much consistency, the Δ_{a-d} values exhibit the same pleasing trends as in Table 6.2. This suggests that roll error, e_r, is not a significant contributor to the overall attitude bias, σ_{att}°.

Table 6.4: *Attitude errors predicted assuming 0° Roll error for Patagonia, Equatorial regions, and Western Greenland. Attitude errors estimated assuming a constant interbeam bias.*

Data Set	Axis	Patagonia			Equatorial			Greenland		
		Asc	Desc	Δ_{a-d}	Asc	Desc	Δ_{a-d}	Asc	Desc	Δ_{a-d}
S4-S5	R									
w/o roll	P	-.27	-.40	.13	-.38	-.20	-.18	-.30	-.26	-.04
	Y	.15	.02	.13	.25	.11	.14	.48	.26	.22
JD 269-278	R									
w/o roll	P	-.05	-.16	.11	-.18	-.02	-.16	-.15	-.03	-.12
	Y	.27	.11	.16	.32	.15	.17	.59	.43	.16
S18-S19	R									
w/o roll	P	-.12	-.18	.06	-.14	-.08	-.06	-.17	-.04	-.13
	Y	-.89	-.99	.10	-.82	-.95	.13	-.48	-.71	.23
JD 319-328	R									
w/o roll	P	.04	-.04	.08	.06	.10	-.04	.09	.17	-.08
	Y	-1.18	-1.25	.07	-1.07	-1.17	.10	-.88	-.99	.11

In general, trends in Δ_{a-d}Yaw are the strongest. However, several interesting trends in Δ_{a-d}Pitch are also worthy of note. The trends in the Equatorial latitude band have the best consistency followed by those in Patagonian latitude band while those in the Greenland latitude band appear the weakest. This is probably because

three calibration regions were used in the Equatorial latitude band and only one in the other two. Perhaps the Patagonian band's proximity to the Equatorial band leads to some correlation between their attitude errors and thus correspondingly stronger trends in its data.

The Δ_{a-d}Yaw (with roll) of Table 6.2 for the Equatorial region follow a trend in time. In the Equatorial band, data from early in the mission ("S4-S5", "JD 269-278", and "JD 279-288") has a Yaw difference of approximately .19°. Later in the mission ("S18-S19" and "JD 319-328") it decreases to about .15°. In the Patagonian band, a similar trend appears. Early mission Δ_{a-d}Yaw is also about .19° (excluding "JD 279-288") while later mission data is .13°. In the Greenland band, similar data appears, though there are some "outliers". These same trends also appears in Table 6.4 where zero roll is assumed. These observations strongly suggest that the ascending and descending yaw differed throughout the mission.

The Δ_{a-d}Pitch exhibits a similar trend in Table 6.4. Early in the mission, $\Delta_{a-d}\text{Pitch} \approx .12°$ over Patagonia and $\approx -.17°$ over Amazon. Later in the mission, its magnitude decreases to .07° and $-.05°$. These trends suggest that the ascending and descending pitch estimates reported by the spacecraft also differed throughout the mission.

Information was later obtained indicating that the spacecraft estimated its attitude using different systems for ascending and descending passes. Based on the results and observations above, it appears that the two systems contain a non-zero residual bias which has time-dependent properties. An investigation by representatives of the Jet Propulsion Laboratory (JPL), developers of NSCAT, in February, 1997 suggested that the attitude determination system used by ADEOS could be subject to errors much larger than originally thought [19]. It was found that the attitude sensor actually used on the spacecraft was not the instrument JPL analysts thought was being used. An expert in satellite attitude control reported that diurnal bias differences in yaw attitude of $> 0.1°$ and in pitch attitude of $\approx 0.2 - 0.3°$ were considered realistic. While the analysis presented in this chapter does not predict absolute attitude errors very well, it does confirm the magnitude of the yaw and pitch diurnal errors estimated by this expert.

Though this technique produces a consistent interbeam bias for several calibration regions, it does not produce consistent results across all latitude bands. The most consistent regions are the members of the Equatorial band. As noted

previously, this is probably due to the fact that three equatorial regions are used and only one each for the other two latitude bands. Recall that this technique estimates one interbeam bias for the entire orbit. A plot of this interbeam bias is found in Figure 6.1. The bias previously implemented by JPL is indicated by a dotted line, the modifications suggested here with a solid line, and the combined result with a dash-dot line.

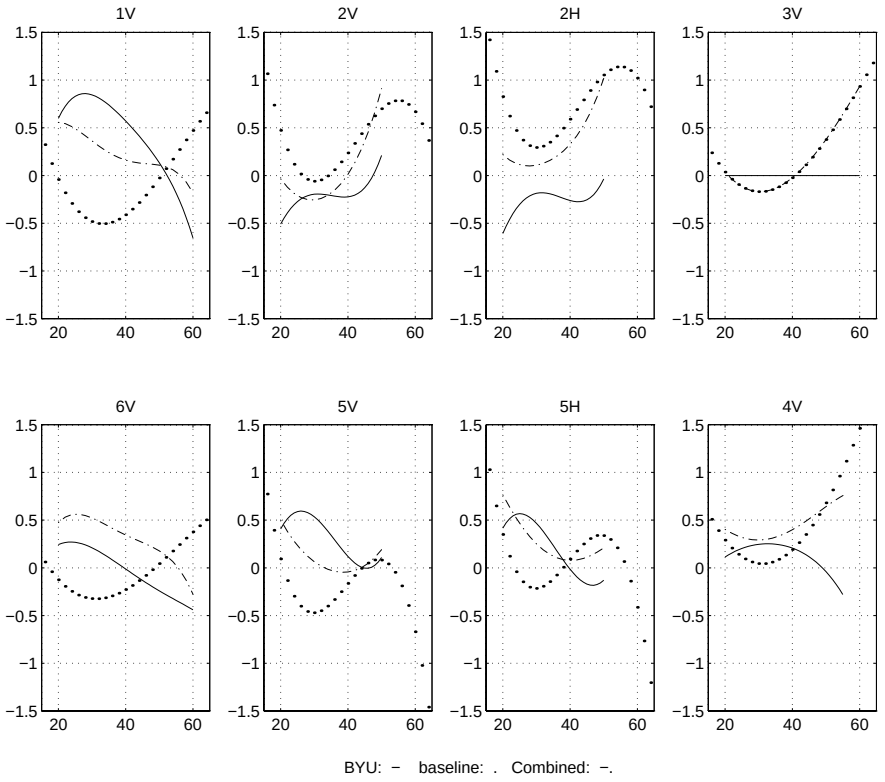

Figure 6.1: *Interbeam bias (normalized to beam 3V) estimated for data set "S18-S19" with the estimation technique of Equation 5.18. This interbeam bias is to be constant over the entire orbit.*

To investigate the quality of the interbeam bias estimated using this technique, the attitude bias corrections, $\Delta\hat{\sigma^\circ}_{att}$, are subtracted from the $\Delta\hat{\sigma^\circ}_{meas}$ to obtain the sum of the predicted interbeam bias , $\hat{\sigma^\circ}_{ibb}$, and the residual error term of Equation 5.6, $\Delta\hat{\sigma^\circ}_{err}$, (recall that this term was assumed to be negligible). Some representative results from different latitude bands are found in Figures 6.2 thru 6.4 of the data set S18-S19. The distinct differences in the ascending and descending passes' interbeam biases (especially on beams 5V and 5H) are much larger than what can be considered reasonable for implementation in the NSCAT data processing algorithms.

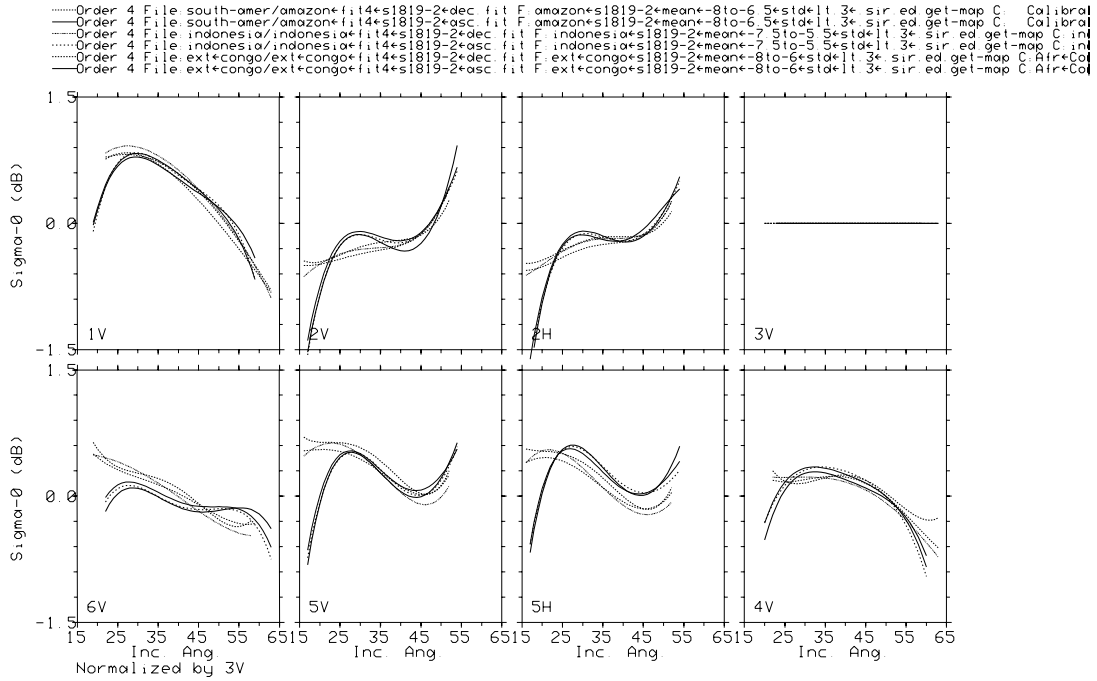

Figure 6.2: *Equatorial regions interbeam bias (+ error) after attitude bias removal (normalized to beam 3V). Attitude error calculated using Patagonia, Equatorial, and Western Greenland regions.*

This technique used the same interbeam bias for both ascending and descending passes, thus the $\Delta\hat{\sigma^{\circ}}_{err}$ residual error term must be significantly different for the ascending and descending passes. Subtracting the predicted interbeam bias reveals the residual error $\Delta\hat{\sigma^{\circ}}_{err}$. The results are plotted in Figures 6.5 thru 6.7. The residual error is greater than 0.1° for much of the elevation angles of interest for both ascending and descending. In particular, for Patagonia and Western Greenland the residual error is extremely large. This indicates that constraints assumed on the system may be too restraining for this simple estimation technique. This hypothesis may be tested by relaxing some of the constraints to see if the technique can produce better interbeam bias estimates.

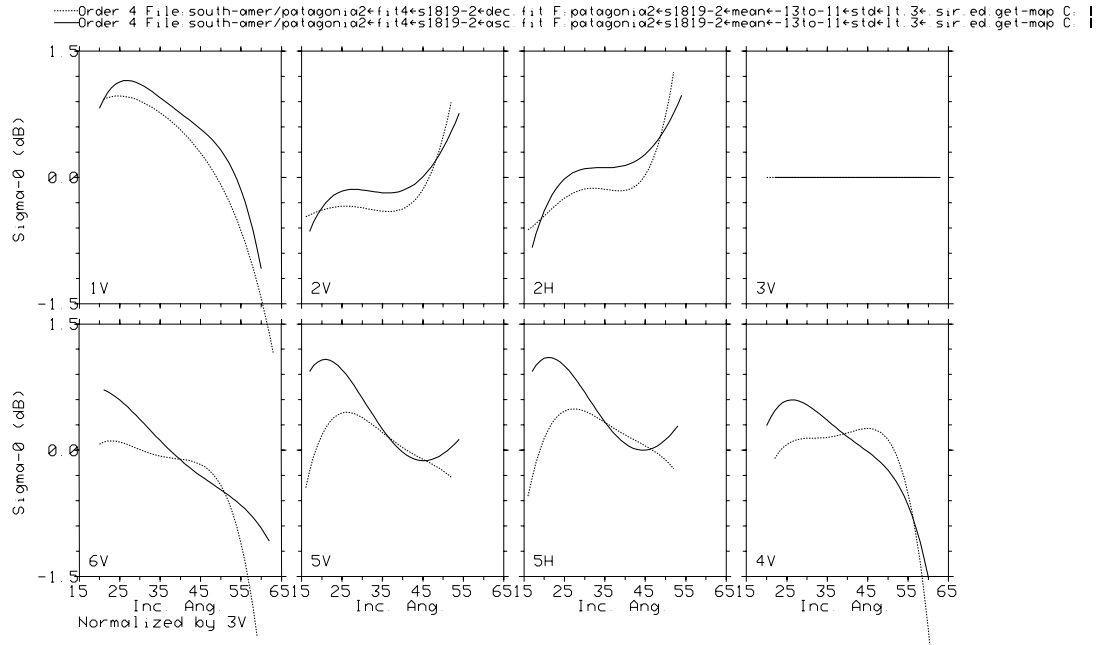

Figure 6.3: *Patagonia region interbeam bias (+ error) after attitude bias removal (normalized to beam 3V). Attitude error calculated using Patagonia, Equatorial, and Western Greenland regions.*

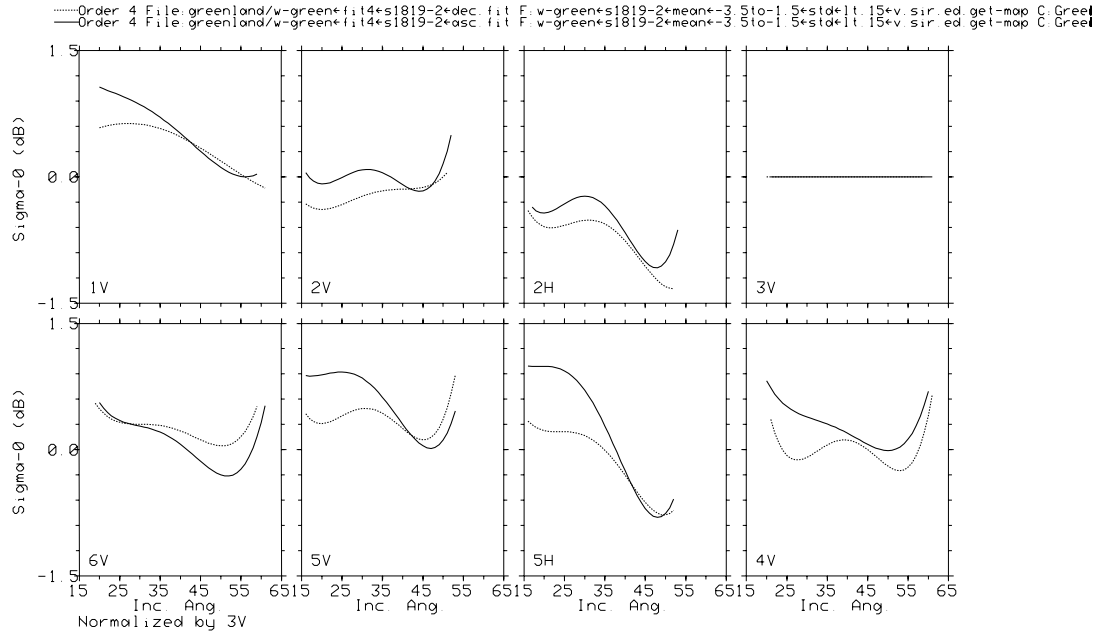

Figure 6.4: *Western Greenland region interbeam bias (+ error) after attitude bias removal (normalized to beam 3V). Attitude error calculated using Patagonia, Equatorial, and Western Greenland regions.*

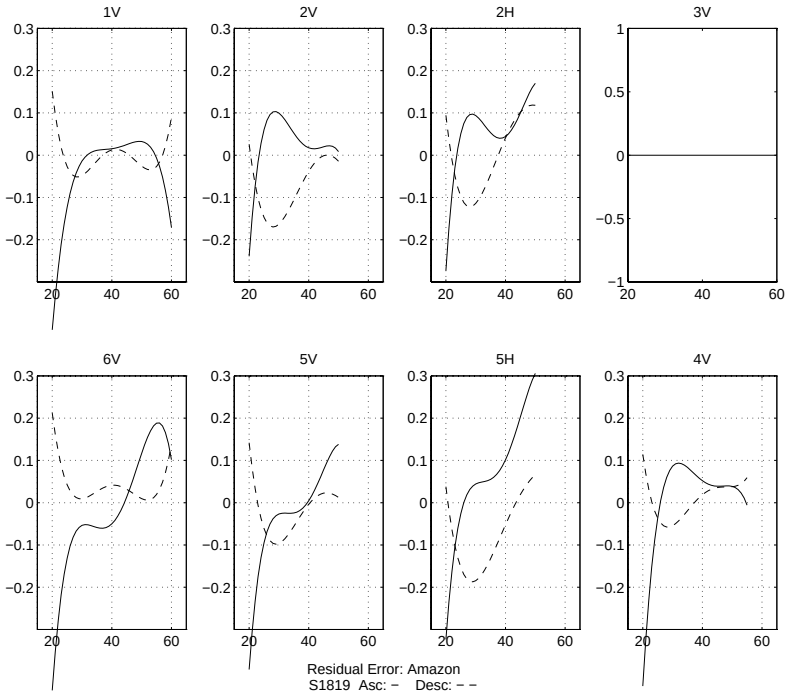

Figure 6.5: *Residual error (normalized to beam 3V) for the Amazon region after both the estimated interbeam bias and attitude bias corrections are removed (data set "S18-S19").*

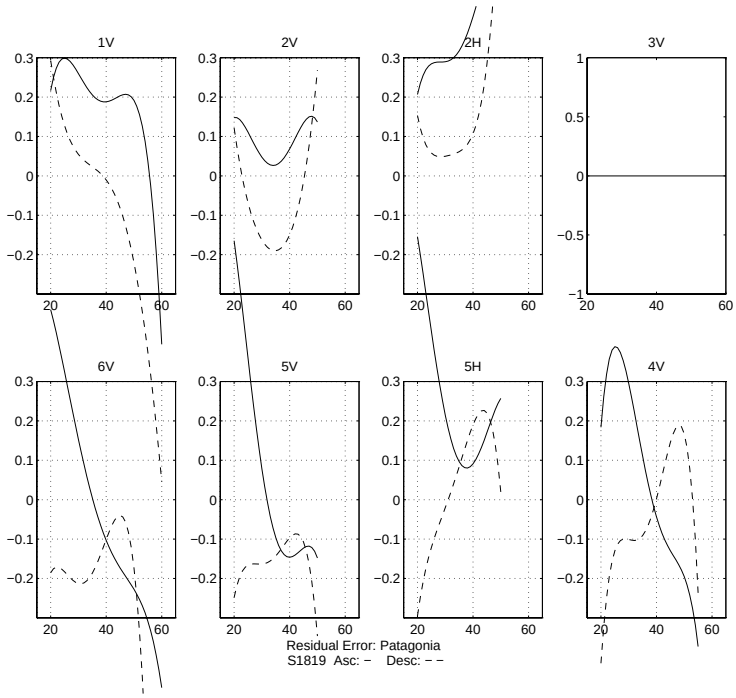

Figure 6.6: *Residual error (normalized to beam 3V) for the Patagonian region after both the estimated interbeam bias and attitude bias corrections are removed (data set "S18-S19").*

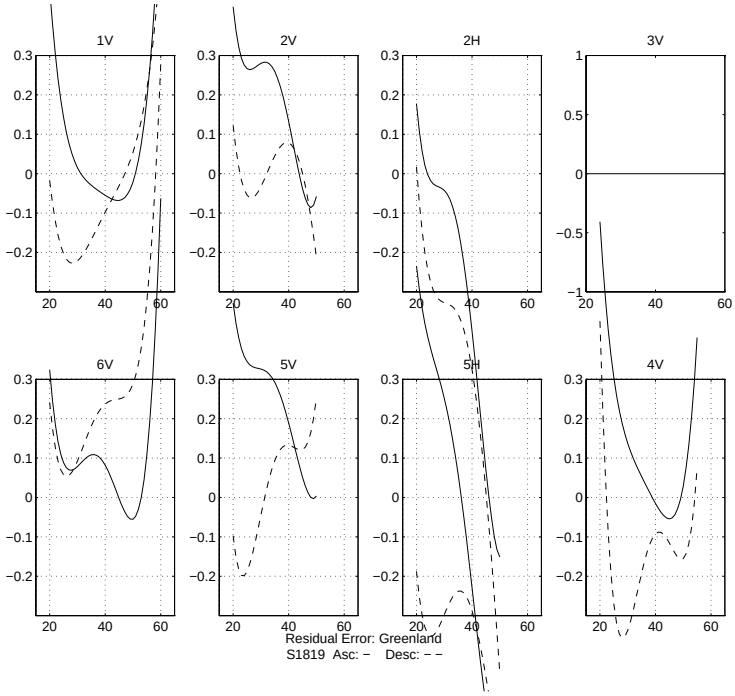

Figure 6.7: *Residual error (normalized to beam 3V) for the Western Greenland region after both the estimated interbeam bias and attitude bias corrections are removed (data set "S18-S19").*

6.3 Variations of the Technique and Corresponding Results

Because the results of the primary estimation technique do not provide completely satisfactory interbeam bias estimates, the same basic theory is re-applied using slightly different assumptions to see if so doing would yield improved results. The first variation is to estimate attitude errors using only the Equatorial regions and then apply these estimates to the other regions. The second variation allows the ascending and descending passes to have different interbeam biases.

6.3.1 Single Latitude Band Attitude Error Estimation Variation

In this subsection, a different method of estimating the attitude error is presented. It is a derivative of the primary technique with the main difference being it only uses data from one latitude band.

Rearranging Equation 5.7,

$$P_{ibb}(c,b) \approx \Delta P_{meas}(c,b) - \Delta P_{att}(c,b), \qquad b = 1, \ldots, 6, 8. \tag{6.1}$$

Because the interbeam bias is assumed constant for ascending and descending passes, the r.h.s. of Equation 6.1 may be equated for ascending and descending passes.

$$\Delta P_{meas,asc}(c,b) - \Delta P_{att,asc}(c,b) \;=\; \Delta P_{meas,desc}(c,b) - \Delta P_{att,desc}(c,b)$$

Rearranging and applying Equation 5.12,

$$\begin{aligned}
\Delta P_{meas,asc}(c,b) - \Delta P_{meas,desc}(c,b) &= \Delta P_{att,asc}(c,b) - \Delta P_{att,desc}(c,b) \qquad (6.2)\\
\text{or,}& \\
\Delta P_{meas,a-d}(c,b) &= \Delta P_{att,a-d}(c,b) \qquad (6.3)\\
&= \Delta m_{r,asc}(c,b)\cdot e_{r,asc} + \Delta m_{p,asc}(c,b)\cdot e_{p,asc}\\
&\quad +\Delta m_{y,asc}(c,b)\cdot e_{y,asc} - \Delta m_{r,desc}(c,b)\cdot e_{r,desc}\\
&\quad -\Delta m_{p,desc}(c,b)\cdot e_{p,desc} - \Delta m_{y,desc}(c,b)\cdot e_{y,desc}\,.
\end{aligned}$$

To find the least squares estimate of the attitude error form the matrix equation

$$\overline{\Delta P_{meas,a-d}} = \mathbf{M}'\overline{E} \qquad (6.4)$$

where

$$\begin{aligned}
\overline{\Delta P_{meas,a-d}} &= [\Delta P_{meas,a-d}(0,1)\ \cdots\ \Delta P_{meas,a-d}(0,6)\ \Delta P_{meas,a-d}(0,8)\ \cdots \qquad (6.5)\\
&\quad \cdots\ \Delta P_{meas,a-d}(4,1)\ \cdots\ \Delta P_{meas,a-d}(4,6)\ \Delta P_{meas,a-d}(4,8)]^{\mathbf{T}},\\
\overline{E} &= [e_{r,asc}\ e_{p,asc}\ e_{y,asc}\ e_{r,desc}\ e_{p,desc}\ e_{y,desc}]^{\mathbf{T}}, \qquad (6.6)
\end{aligned}$$

and

$$
\mathbf{M}' = \left[\begin{array}{ccc}
\Delta m_{r,asc}(0,1) & \Delta m_{p,asc}(0,1) & \Delta m_{y,asc}(0,1) \\
\vdots & \vdots & \vdots \\
\Delta m_{r,asc}(0,6) & \Delta m_{p,asc}(0,6) & \Delta m_{y,asc}(0,6) \\
\Delta m_{r,asc}(0,8) & \Delta m_{p,asc}(0,8) & \Delta m_{y,asc}(0,8) \\
\vdots & \vdots & \vdots \\
\vdots & \vdots & \vdots \\
\Delta m_{r,asc}(4,1) & \Delta m_{p,asc}(4,1) & \Delta m_{y,asc}(4,1) \\
\vdots & \vdots & \vdots \\
\Delta m_{r,asc}(4,6) & \Delta m_{p,asc}(4,6) & \Delta m_{y,asc}(4,6) \\
\Delta m_{r,asc}(4,8) & \Delta m_{p,asc}(4,8) & \Delta m_{y,asc}(4,8)
\end{array}\right. \tag{6.7}
$$

$$
\left.\begin{array}{ccc}
-\Delta m_{r,desc}(0,1) & -\Delta m_{p,desc}(0,1) & -\Delta m_{y,desc}(0,1) \\
\vdots & \vdots & \vdots \\
-\Delta m_{r,desc}(0,6) & -\Delta m_{p,desc}(0,6) & -\Delta m_{y,desc}(0,6) \\
-\Delta m_{r,desc}(0,8) & -\Delta m_{p,desc}(0,8) & -\Delta m_{y,desc}(0,8) \\
\vdots & \vdots & \vdots \\
\vdots & \vdots & \vdots \\
-\Delta m_{r,desc}(4,1) & -\Delta m_{p,desc}(4,1) & -\Delta m_{y,desc}(4,1) \\
\vdots & \vdots & \vdots \\
-\Delta m_{r,desc}(4,6) & -\Delta m_{p,desc}(4,6) & -\Delta m_{y,desc}(4,6) \\
-\Delta m_{r,desc}(4,8) & -\Delta m_{p,desc}(4,8) & -\Delta m_{y,desc}(4,8)
\end{array}\right] .
$$

Note: $\mathbf{M}'$ has 6 columns and 35 rows. (6.8)

To obtain the least squares estimate of $\overline{\Delta P_{att,a-d}} = \overline{\Delta P_{meas,a-d}}$, use the pseudo-inverse of $\mathbf{M}'$, $\mathbf{M}'^{\dagger}$, to obtain

$$
\widehat{\overline{E}} = \mathbf{M}'^{\dagger}\, \overline{\Delta P_{meas,a-d}}\,. \tag{6.9}
$$

While additional regions may be added to Equations 6.4 thru 6.8, they must (unlike the original method) all be from the same latitude band. However, for estimating just one latitude band, this technique is simpler to expand to multiple regions.

6.3.2 Results of the Single Latitude Band Attitude Error Estimation Variation

The middle three columns of Table 6.5 list the attitude errors predicted for the Equatorial latitude band ($-10°$ to $5°$) when all three regions in this band (Amazon, Congo, and Indonesia) are used. Similar attitude error trends appear here as in the original technique. While the nominal values of this table appear to vary without pattern, again notice the strong stability in the Δ_{a-d} values for pitch and yaw. These differences are approximately $-0.40°$ and $+0.20°$ for the earlier time period of "S4-S5" and "JD 269-278". For the later data sets, the differences are exactly $-0.22°$ and $+.22°$. This indicates that the bias between ascending and descending passes is changing relatively rapidly for pitch, but very slowly for yaw. Again, this result confirms the suspicions of JPL's attitude expert.

Table 6.5: *Attitude errors predicted using calibration regions from the Equatorial latitude band only.*

Data Set	Axis	Equatorial			Equatorial w/o roll		
		Asc	Desc	Δ_{a-d}	Asc	Desc	Δ_{a-d}
S4-S5	R	1.84	2.96	-1.12			
	P	-.55	-.16	-.39	.05	.17	-.12
	Y	1.53	1.33	.20	.62	.46	.16
JD 269-278	R	1.89	3.24	-1.35			
	P	-.55	-.14	-.41	.13	.26	-.13
	Y	1.25	1.04	.19	.35	.19	.16
S18-S19	R	1.58	2.27	-.69			
	P	-.15	.07	-.22	.27	.28	-.01
	Y	.98	.76	.22	.14	-.04	.18
JD 319-328	R	1.83	2.39	-.56			
	P	-.06	.16	-.22	.36	.35	.01
	Y	1.34	1.12	.22	.33	.16	.17

The roll error estimates and Δ_{a-d} values, as in the primary method, take on several absurdly large values and do not exhibit any consistent trend. Suspecting that the roll error is being used as a "fitting parameter", the roll error is again set to zero. The results of this experiment are in the right-hand three columns of Table 6.5. The same distinct trend in the pitch and yaw Δ_{a-d} values appears: the bias between ascending and descending passes changes rapidly for pitch and slowly for yaw.

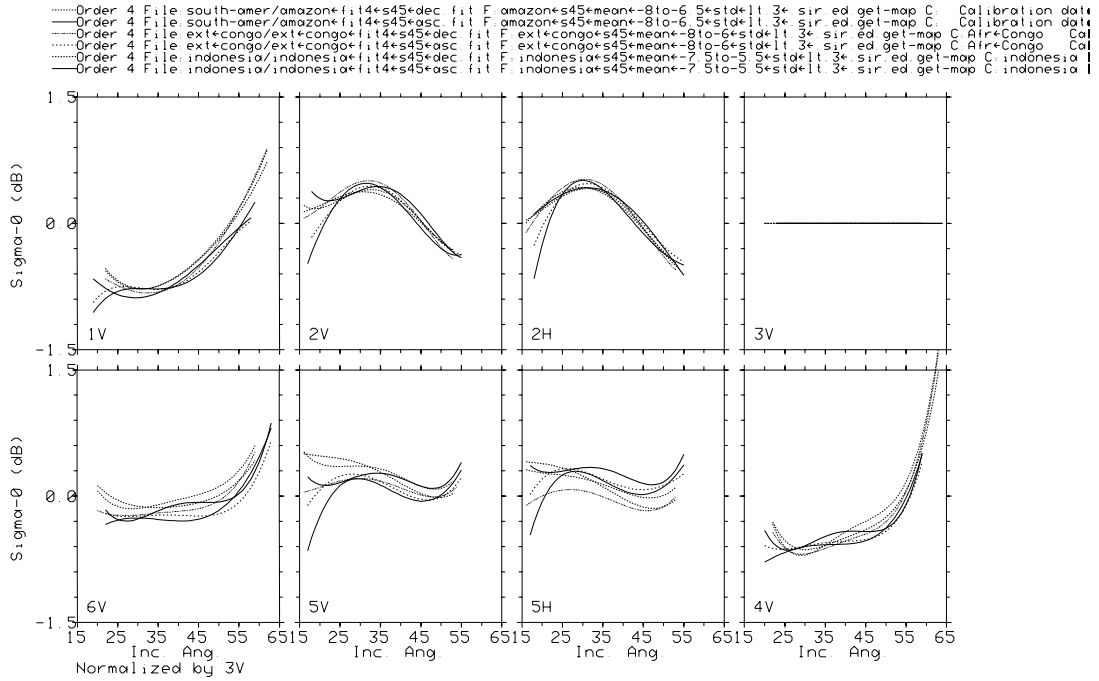

Figure 6.8: *Equatorial regions' interbeam bias (normalized to beam 3V) after attitude bias removal. Attitude error calculated using only Equatorial regions.*

While these Equatorial band attitude error results seemed encouraging, when applied to the other latitude bands (Patagonia and Western Greenland), the results were not as good as the primary technique. Figure 6.8 plots the interbeam bias (plus residual error) for the Equatorial regions. We note all three regions have similar curves, for both ascending and descending passes, as the theory predicts. Figures 6.9 and 6.10 plot the interbeam bias (plus residual error) for Patagonia and Greenland when the attitude error estimated by the Equatorial regions is applied. Unfortunately, the ascending and descending interbeam bias curves differ significantly from each other and from the Equatorial curves of Figure 6.8. This implies different interbeam biases for the different latitude bands which does not seem reasonable. In a final effort to obtain good interbeam bias and attitude error estimates, different interbeam biases are next allowed for ascending and descending passes.

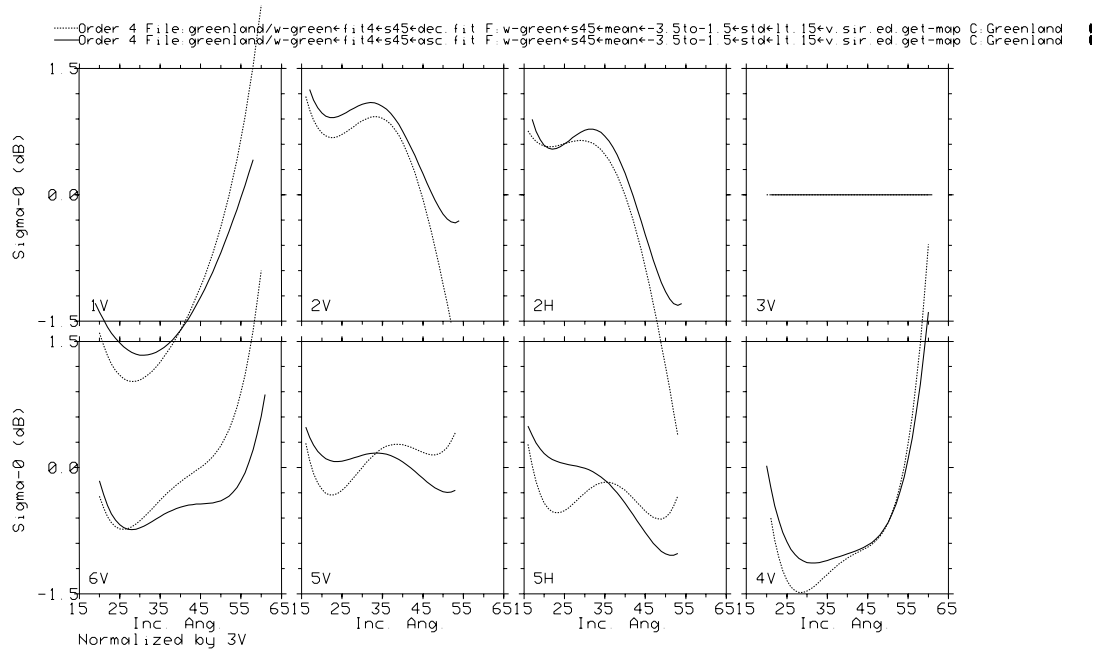

Figure 6.9: *Western Greenland interbeam bias (normalized to beam 3V) after attitude bias removal. Attitude error calculated using only Equatorial regions.*

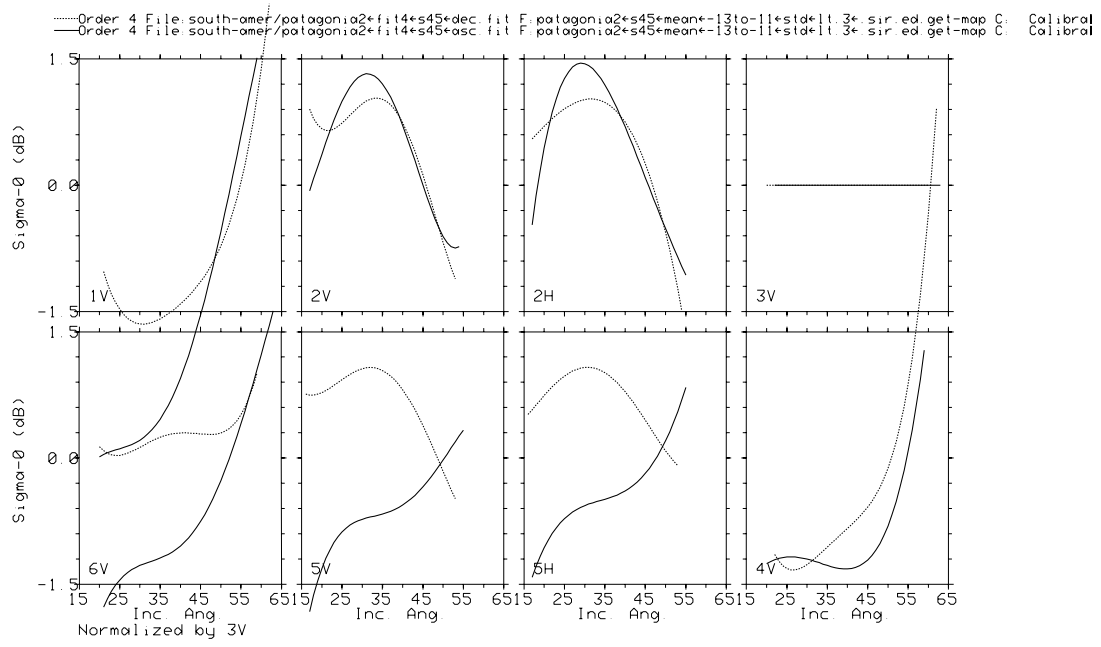

Figure 6.10: *Patagonia interbeam bias (normalized to beam 3V) after attitude bias removal. Attitude error calculated using only Equatorial regions.*

6.3.3 Another Variation: Different Interbeam Biases for Ascending and Descending Passes

The technique of this subsection estimates different interbeam biases for the ascending and descending passes. Two possible justifications for this assumption are, 1) the interbeam bias may vary over a 24 hour period due to diurnal variations of the surface's σ° response, and 2) the temperature of the NSCAT instrument may vary when it is in and out of the Earth's shadow causing different antenna and instrumental responses.

To develop governing equations for this variation, two modifications to Equations 5.14 thru 5.19 are necessary. The matrix $\mathbf{M}$ of Equation 5.17 must be modified. Because separate interbeam balances are sought for ascending and descending passes, a separate set of identity and zero sub-matrices is necessary for each. Second, the vector $\bar{B}$ must have a second set of $P_{ibb}(c,b)$ elements included in order to hold values for the ascending and descending passes' interbeam biases.

Table 6.6 lists the attitude errors estimated by this procedure. The attitude error estimates produced when roll error is restricted to zero are listed in Table 6.7.

Table 6.6: *Attitude errors predicted for Patagonia, Equatorial regions, and Western Greenland. Attitude errors estimated simultaneously with a different interbeam bias for ascending and descending passes.*

Data Set	Axis	Patagonia			Equatorial			Greenland		
		Asc	Desc	Δ_{a-d}	Asc	Desc	Δ_{a-d}	Asc	Desc	Δ_{a-d}
S4-S5	R	3.4	-10.0	13.4	4.3	-6.9	11.2	4.8	-6.8	11.6
	P	0.1	0.1	0.0	-0.1	0.1	-0.2	0.0	0.2	-0.2
	Y	-4.7	-3.8	-0.9	-4.5	-3.6	-0.9	-4.3	-3.5	-0.8
JD 269-278	R	3.5	-7.0	10.5	5.3	-5.4	10.7	4.4	-6.2	10.6
	P	.3	.3	0.0	0.0	.3	-.3	.2	.4	-.2
	Y	-7.9	-4.6	-3.3	-7.6	-4.5	-3.1	-7.5	-4.3	-3.2
S18-S19	R	2.4	-8.1	10.5	5.4	-4.5	9.9	5.2	-6.2	11.4
	P	2.2	-.6	2.8	1.9	-.7	2.6	1.8	-.6	2.4
	Y	-11.6	-8.7	-2.9	-11.2	-8.5	-2.7	-11.0	-8.6	-2.4
JD 319-328	R	4.5	-11.7	16.2	2.4	-8.1	10.5	3.2	-8.6	11.8
	P	1.5	1.1	.4	1.4	1.0	.4	1.3	1.2	.1
	Y	-7.9	-11.0	3.1	-7.6	-10.7	3.1	-7.5	-10.8	3.3

There are two very evident features about the data in these tables. First, the attitude error values are extremely large, approximately an order of magnitude larger than those produced by the previous two techniques. The interbeam bias

Table 6.7: *Attitude errors predicted with 0° roll error for Patagonia, Equatorial regions, and Western Greenland. Attitude errors estimated simultaneously with a different interbeam bias for ascending and descending passes.*

Data Set	Axis	Patagonia			Equatorial			Greenland		
		Asc	Desc	Δ_{a-d}	Asc	Desc	Δ_{a-d}	Asc	Desc	Δ_{a-d}
S4-S5	R									
w/o roll	P	-0.2	0.6	-0.8	-0.2	0.7	-0.9	-0.2	0.6	-0.8
	Y	-2.0	-5.4	3.4	-1.8	-5.2	3.4	-1.6	-5.2	3.6
JD 269-278	R									
w/o roll	P	-1.4	1.1	-2.5	-1.6	1.2	-2.8	-1.6	1.1	-2.7
	Y	-5.0	-4.6	-.4	-4.9	-4.4	-.5	-4.7	-4.3	-.4
S18-S19	R									
w/o roll	P	.7	1.0	-.3	.7	1.0	-.3	.6	.9	-.3
	Y	-7.8	-8.8	1.0	-7.6	-8.6	1.0	-7.4	-8.7	1.3
JD 319-328	R									
w/o roll	P	1.5	2.1	-.6	1.5	2.1	-.6	1.4	2.0	-.6
	Y	-5.5	-12.2	6.7	-5.3	-11.9	6.6	-5.2	-12.1	6.9

estimates associated with these attitude error estimates are also an order of magnitude larger than than that of the other two techniques.

Second, the nominal and differential attitude error estimates are, in almost all cases (except for roll), very similar for all of the latitude bands across a given data set. This had not been observed for the other techniques, though it seems rather reasonable. As an interesting twist, the patterns seen in the other techniques do not appear here. For instance, the roll/no-roll columns do not correspond and there are few if any correlations between parameters of different data sets.

While the extremely huge attitude errors and interbeam biases estimated by this technique declare them unusable, it does produce very consistent attitude errors within each data set. Finally, note that again in this technique, even with its loosened constraints on ascending and descending interbeam bias errors, significant non-zero Δ_{a-d} values are obtained.

6.4 Summary

This chapter has presented the attitude error and interbeam bias estimates produced by the model of Equations 5.14 thru 5.19. While the absolute attitude errors do not appear to follow discernible patterns, the difference between the ascending and descending passes' attitude errors, Δ_{a-d}, does have a distinct trend. This difference

changes markedly in yaw from the early data sets to the later ones. It also demonstrates a change in pitch. A JPL attitude expert suggested that diurnal variations in attitude would be significant. The magnitude of Δ_{a-d} confirms his assessment.

Following the original technique's results, the results of two variations with slightly different assumptions were presented. Both variations demonstrate significant differences in the attitude errors and interbeam biases for the ascending and descending passes. These differences support the conclusions of the original technique. However, the variation techniques demonstrate little, if any, improvement in the attitude error estimates. Thus, it appears the attitude errors and interbeam biases estimated by the original technique are representative of the estimate quality of which the general method is capable.

Chapter 7

CONCLUSIONS

This chapter summarizes the efforts of this thesis. A list of contributions made to the field of spaceborne scatterometry is presented. Suggested topics for further research in spaceborne scatterometer calibration conclude this chapter.

7.1 General Summary

This thesis has presented an approach for the calibration of and attitude error estimation for a spaceborne scatterometer using measurements over land. A methodology for selecting land regions to use as calibration targets has also been presented. The calibration approach is based on the technique previously developed by Long and Skouson [3]. This thesis extends their work in two important ways.

First, measurement data from multiple calibration regions and multiple latitude bands are simultaneously used to form the estimates. This extension forces the interbeam bias estimates produced by the algorithm to be constant throughout the instrument's orbit. An alternative approach explored the possibility of different interbeam biases for the ascending and descending passes.

Second, a simple approach to estimating the scatterometer's host spacecraft's attitude error has been presented. This approach separated the measurement bias caused by attitude error into contributions from roll, pitch, and yaw error. The capability of the technique to estimate the absolute attitude errors was very limited. The attitude angle errors produced were not consistent from data set to data set (*i.e.*, in time). However, the difference between the ascending and descending errors, Δ_{a-d}, for pitch and yaw displayed a distinct trend under every variation of the approach analyzed. The magnitude of these Δ_{a-d} values consistently change over the 3-4 month period of the data set. Further, their magnitudes confirm the assessment provided to JPL by an expert in satellite attitude control.

7.2 Contributions

This thesis has made three primary contributions to the field of spaceborne scatterometry. First, a new methodology for selecting calibration regions has been

developed. Second, the technique of Long and Skouson [3] has been applied to an on-line, uncalibrated scatterometer. Third, an approach to estimating a spaceborne scatterometer's attitude using its measurements has been developed and applied. These contributions have been important in NSCAT's calibration/validation check-out phase and will be of interest in future calibration efforts.

The methodology for selecting calibration regions as presented in Chapter 3 is a contribution which may be useful in future spaceborne scatterometer efforts. Finding regions to use in a calibration effort is an important first step in the process. Using regions which have backscatter responses that are stable in time and constant over large spatial areas is a desirable approach. This methodology provides a means of identifying such areas. During the course of this work, areas previously identified as good calibration regions have been confirmed as such (*i.e.*, the Amazon and Congo rainforests [3,8]). Further, new regions have been identified and successfully used in this thesis (*i.e.*, Western Greenland and Patagonia). All of the regions selected by this methodology are also reasonable choices from a scattering point of view. This methodology also has application in the larger task of cataloging the backscatter properties of the land regions of the Earth.

The application of the calibration method of Long and Skouson [3] has been applied for the first time to an on-line scatterometer during its calibration/validation check-out phase. The results obtained using this method were influential in determining the calibration corrections applied to NSCAT in both the preliminary and final calibration assessments. Future multiple-antenna scatterometers may find this technique of value for their calibration requirements.

The calibration technique has been extended to estimate the scatterometer's attitude using its measurements over calibration regions. There has never been an attempt to use scatterometer measurements to estimate the spacecraft's attitude. While the effort in this thesis was not entirely successful, it was able to confirm the magnitude of diurnal yaw and pitch variations estimated by a satellite attitude expert [19]. This suggests that the usefulness of the information content in scatterometer measurements over land regions is worthy of further investigation.

7.3 Future Work

As suggested in the previous section, the major contributions of this thesis all lead to possible areas of future research. With the approaching launch of the

QuickScat scatterometer in November, 1998 and also the SeaWinds scatterometer in 2000, the techniques developed and applied here may be adapted and refined for use in their calibration phases.

The methodology for selecting calibration regions could be extended in many directions. Probably most useful would be to form a database of the backscatter mean and standard deviation of the entire world over time windows appropriate for discovering seasonal and interannual variations. The process of forming masks could also be automated or applied using pattern recognition techniques with vegetation databases instead of visual inspection. A combination of these two extensions might monitor changes in vegetation regions over time.

The method of estimating the spacecraft's attitude using the scatterometer's measurements may be refined in several ways. As mentioned during the derivation, developing a method to use *weighted* least squares instead of ordinary least squares would minimize the estimates' dependence on erroneous measurements. The current method is a linear approach. Removing the assumptions and simplifications which allow this linearity will likely lead to attitude estimates of higher quality. Of course, the estimation procedure will become non-linear and more complex in the process. One such simplification is assuming the attitude bias contributed from each axis (roll, pitch, and yaw) is independent of the other axes. They should be combined using the appropriate rotation scaling matrices. Another approach may be to calculate the attitude bias by calculating the change in the X-factor for a given attitude error. A more rigorous approach to estimating the attitude may produce attitude error estimates which are more consistent than those obtained with the method of this thesis.

Bibliography

[1] F.M. Naderi and M.H. Freilich and D.G. Long, "Spaceborne Radar Measurement of Wind Velocity Over the Ocean—An Overview of the NSCAT Scatterometer System," *Proceedings of the IEEE*, vol. 79, no. 6, pp. 850–866, June 1991.

[2] G.B. Skouson, "Calibration of SEASAT Scatterometer using Tropical Rainforest," Master's thesis, Brigham Young University, 1992.

[3] D.G. Long and G.B. Skouson, "Calibration of Spaceborne Scatterometers using Tropical Rain Forests," *IEEE Transactions on Geoscience and Remote Sensing*, vol. 34, no. 2, pp. 413–424, March 1996.

[4] F.T. Ulaby, R.K. Moore, and A.K. Fung, *Microwave Remote Sensing: Active and Passive*, vol. I, II, Addison-Wesley Pub. Co., 1981, 1982, vol. III, Artech House, 1986.

[5] D.G. Long, C.-Y. Chi, and F.K. Li, "The Design of an Onboard Digital Doppler Processor for a Spaceborne Scatterometer," *IEEE Transactions on Geoscience and Remote Sensing*, vol. 26, no. 6, pp. 869–878, November 1988.

[6] E.M. Bracalente, D.H. Boggs, W.L. Grantham, and J.L. Sweet, "The SASS Scattering Coefficient σ° Algorithm," *IEEE Journal of Oceanic Engineering*, vol. OE-5, no. 2, pp. 145–154, April 1980.

[7] P. Lecomte and E.P.W. Attema, "Calibration and Validation of the ERS-1 Wind-Scatterometer," *Proceedings of the* 1^{st} *ERS-1 Symposium*, 1993, pp. 19–29.

[8] R.G. Kennett and F.K. Li, "Seasat over Land Scatterometer Data, Part II: Selection of Extended Area Land-target Sites for the Calibration of Spaceborne Scatterometers," *IEEE Transactions on Geoscience and Remote Sensing*, vol. 27, pp. 779–788, 1989.

[9] R.G. Kennett and F.K. Li, "Seasat over Land Scatterometer Data, Part I: Global Overview of the Ku-band Backscatterer Coefficients," *IEEE Transactions on Geoscience and Remote Sensing*, vol. 27, pp. 592–605, 1989.

[10] E. Mougin, A. Lopes, P.L. Frison, and C. Proisy, "Preliminary Analysis of ERS-1 Wind Scatterometer Data over Land Surfaces," *International Journal of Remote Sensing*, vol. 16, no. 2, pp. 391–398, 1995.

[11] D.G. Long, P.J. Hardin, and P.T. Whiting, "Resolution Enhancement of Spaceborne Scatterometer Data," *IEEE Transactions on Geoscience and Remote Sensing*, vol. 31, no. 3, pp. 700–715, May 1993.

[12] D.G. Long and P. J. Hardin, "Vegetation Studies of the Amazon Basin Using Enhanced Resolution Seasat Scatterometer Data," *IEEE Transactions on Geoscience and Remote Sensing*, vol. 32, no. 2, pp. 449–460, March 1994.

[13] C.J. Wilson III and D.G. Long, "Analysis of the Canadian Boreal Forest using Enhanced Resolution ERS-1 Scatterometer Imagery," *Proceedings of the International Geoscience and Remote Sensing Symposium*. IEEE Geoscience and Remote Sensing Society, 1996, vol. 1, pp. 218–220, IEEE.

[14] D.S. Early and D.G. Long, "Enhanced Resolution Imaging from Irregular Samples," *Proceedings of the International Geoscience and Remote Sensing Symposium*, Singapore, Aug. 4-8 1997.

[15] I.J. Birrer, E.M. Bracalente, G.J. Dome, J. Sweet, and G. Berthold, "σ° signature of the amazon rain forest obtained from the seasat scatterometer," *IEEE Transactions on Geoscience and Remote Sensing*, vol. 20, no. 1, pp. 11–17, January 1982.

[16] D.G. Long and M.R. Drinkwater, "Greenland ice-sheet surface properties observed by the seasat-a scatterometer at enhanced resolution," *Journal of Glaciology*, vol. 40, no. 135, pp. 213–230, 1994.

[17] V. Hsaio, "NSCAT X-Factor Attitude Corrections," Binary Data Files, December 1996.

[18] G. Faist and W.-P. Lee, "NASA Scatterometer (NSCAT) Science Data Processing System Level 1.5 Data Software Interface Specification (SIS-2), Revision C (597-512-22)," Jet Propulsion Laboratory, November 1996.

[19] C.J. Wilson III, Author's notes from JPL Teleconference, February 1997.